

Contents

| | | |
|----------|--|-----------|
| 1 | Introduction | 2 |
| 2 | Damage localization during an earthquake | 4 |
| 2.1 | Pulverization: an extreme case of dynamic damage | 5 |
| 2.1.1 | Can we reproduce pulverization ? | 5 |
| 2.1.2 | What are the conditions for pulverizing rocks ? | 7 |
| 2.2 | What are the properties of pulverized rocks? | 9 |
| 2.3 | Perspectives: Dynamic damage near an active fault | 9 |
| 3 | Variation of hydraulic properties across active faults | 10 |
| 4 | Localization process at the onset of coseismic slip | 11 |
| A | Rock pulverization at high strain rate near the San Andreas fault / Nature Geosciences, 2009 | 12 |
| B | High strain rate damage of Carrara marble / Geophysical Research Letters, 2011 | 17 |
| C | Effect of initial damage on rock pulverization along faults / Pure and Applied Geophysics, 2012 | 24 |

Chapter 1

Introduction

Natural active faults have a variety of structures (*Faulkner et al.*, 2010; *Caine et al.*, 1996). They can be composed of a single very localized strand (*Chester and Logan*, 1986) or be formed of a series of anastomosing fault surface (?) that isolate strong lenses within a fault (*Candela and Renard*, 2012)

The structure of a fault has an effect on several properties:

- Their propensity to fail. The gouge of last slipping strand can be substantially weak, but it is also consolidated by healing, sometimes being stronger than prior to slip. Healing of this zone depends on the fluid geochemistry, that can be changed by enhanced permeability along fault (fault valve effect, (*Sibson*, 1992)). Pressure solution is also enhanced by smaller grain size, that can be due to co-seismic fragmentation (*Doan and Gary*, 2009), and the presence in moderate amount of clay (*Bos et al.*, 2000).
- They strongly affects their transport properties. It is often seen that fractures are found along not in the gouge itself (because it is plastic, full of clay), but in the nearby damage zone (large fractures take a longer time to heal (*Gratier and Gueydan*, 2007; *Gratier et al.*, 2011)).
- This structure induces a different mechanical compliance, not only because of its weak components like clay, but because of this large amount of fractures. Many of the fault gouges found

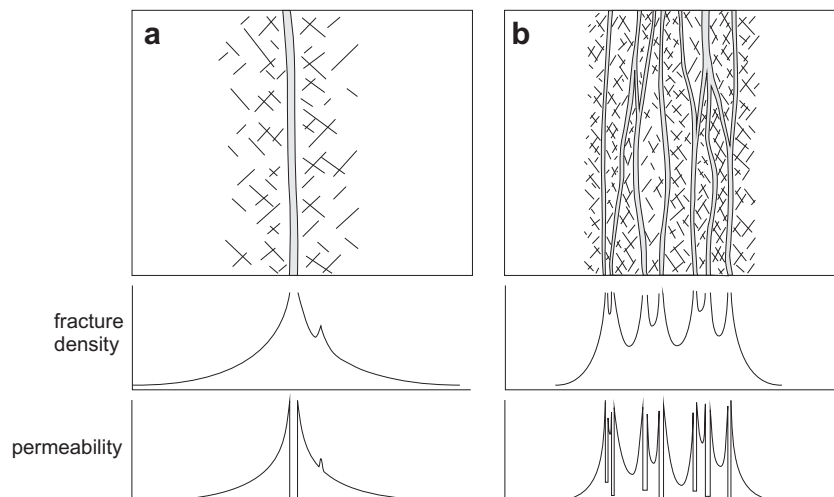


Figure 1.1: Different structures of a fault, either with a single fault core (a) or with multiple fault cores (b). Fault cores are display in light gray color, and fractures are sketched a short straight lines. The structure of the fault would alter the profiles across the fault of fracture density and permeability. From *Faulkner et al.* (2010)

in in-situ conditions (borehole) are often quasi-impervious (Lockner on Nojima, TCDP, San Andreas Fault, Tanikawa on Nankai and J-FAST). This compliance may be key to the sensitivity of fault to static triggering by nearby earthquakes or dynamic triggering by teleseismic waves.

In this report, I focus on better characterizing in situ the structure of fault, primarily their hydraulic properties, and on the creation of this structure. I especially discuss the high strain rate processes, that are expected to occur during slip, or even at the arrival of the seismic waves of the approaching rupture patch, and how they precondition the fault prior to its slip. In particular, I focus on the high strain rate damage, that can induce pulverization, and on the dynamic structuration of a fault gouge during high velocity shear.

Chapter 2

Damage localization during an earthquake

Fault localizes slip within a narrow core filled by fine-grained material named gouge. Around this fault extends a damage zone of variable extension, with a decrease in fracture density with distance from the core. Damage near fault can be generated by several processes [Mitchell and Faulkner, 2009], either statically from the slow extension of the fault, or dynamically during the rupture process.

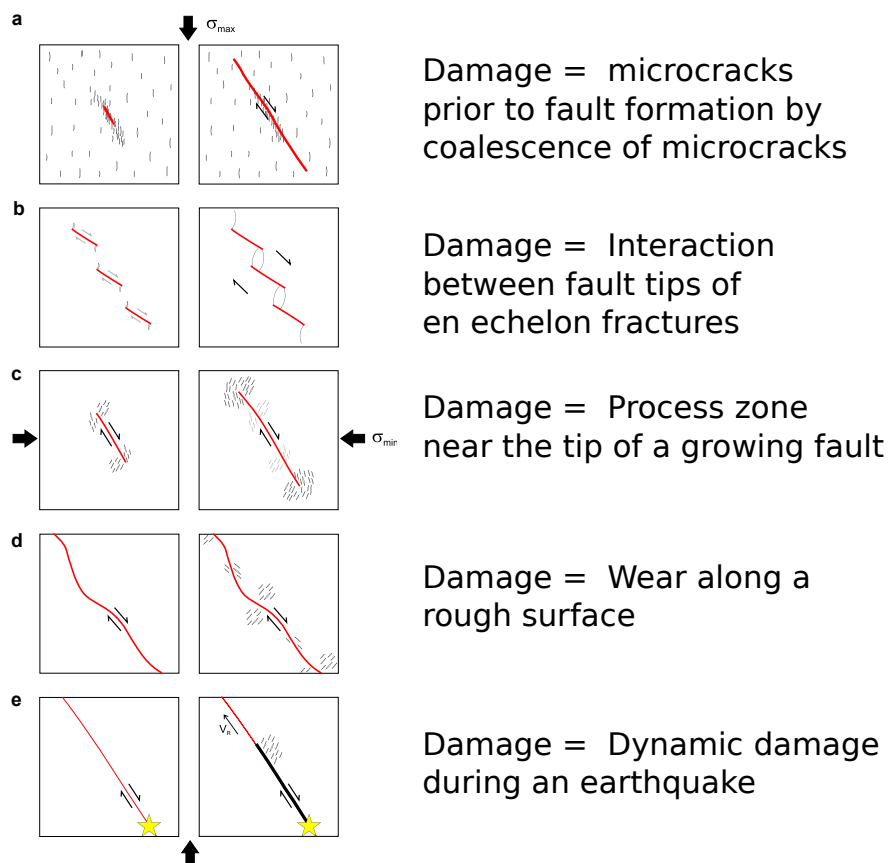


Figure 2.1: Review of 5 models explaining the damage observed around faults. Dynamic damage (model e) would be overprinted with other mechanisms of damage and subsequent fault healing. From *Mitchell and Faulkner* (2009).

Deciphering dynamic damage within natural damage is difficult because of the overprinting of static damage, inherited during the maturation of the fault, and the subsequent healing. The best

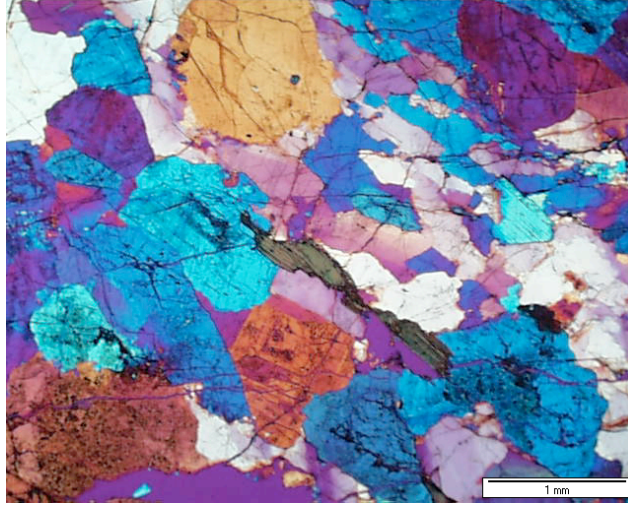


Figure 2.2: Thin section of a pulverized rock sampled near Lake Hughes, along the Mojave segment of the San Andreas Fault. The sample is microfractures, with fractures cutting through grains. The initial grain structure is preserved. Feldspar alteration is present but cannot explain the weakness of the rock. From *Doan and D'Hour* (2012)

location to assess the extent of dynamic damage is a shallow environment – where healing is slow (Gratier) –, near major active faults where large earthquakes are also expected . This is where pulverized rocks have been so far detected.

2.1 Pulverization: an extreme case of dynamic damage

Pulverized rocks is a peculiar form of damage, only recently identified, first near major Californian faults (*Wilson et al.*, 2005; *Dor et al.*, 2006), and observed thereafter on several active faults (Northern Anatolian Fault (*Dor et al.*, 2008), Arima-Akatsuki fault (*Mitchell et al.*, 2011)). It is characterized by an intense microfracturing, with many intragranular fractures, but with little strain recorded, as the initial microstructures are not disturbed. In the field, the sample may look fresh but is easily crumbled by hand. This microfracturing is extensive: zones of pulverized rock extending over several hundred of meters have been reported (*Dor et al.*, 2006; *Mitchell et al.*, 2011)).

Pulverized rocks are surprising because strain has not been localized, as is commonly seen in nature and in laboratory experiments (?). During our research, we hypothesized that high strain rate loading would have inhibited strain localization. Pulverized rocks could therefore be records of previous large earthquakes occurring near the fault.

We define pulverization as the lack of localization along faults. The first experiments we conducted with rocks sampled near the Lake Hughes area, a road outcrop near the San Andreas Fault where intense pulverization was reported (*Dor et al.*, 2006). The experiments were performed in the Ecole Polytechnique at the Laboratoire de Mécanique des Solides in collaboration with Gérard Gary.

To test this hypothesis, we conducted experiments at high strain rate. Several questions were to be answered:

1. Can we reproduce pulverization ?
2. What are the conditions to get pulverization ?

2.1.1 Can we reproduce pulverization ?

We use Split Hopkinson Pressure Bars (SHPB) to load the sample uniaxially at strain rates between 50 /s and 500 /s. At such rate, stress wave propagation has to be taken into account. For instant,

1% strain at 500 /s is reached after 20 μ s. During that time, stress waves propagate over 10 cm in a metal cylinder with P wave velocity of 5000 m/s. In an usual rock mechanics rig – and in the SHPB system –, strain gauges do not record the actual strain experienced by the sample. With the simple geometry of the SHPB apparatus, it is possible to retropropagate waves to the ends of the bars, hence at the edges of the sample, which is not possible in the more complex geometry of an usual rig. That is why SHPB apparatus are commonly used to perform high strain rate experiments (Chen and Song, 2010).

Yes, for crystalline rocks

The first set of experiments we performed was on natural granodioritic samples from the San Andreas Fault, near the Lake Hughes outcrop of pulverized rocks. We took non pulverized rocks sampled at about 100 m from the fault core, and used them as a proxy of the rocks before pulverization: damaged, but only slightly. The uniaxial high strain rate experiments provided only 3 outcomes (Doan and Gary, 2009):

1. the sample was not damaged
2. the sample was split axially in a few fragments, no more than 5. This is the typical damage observed when a rock sample is uniaxially loaded at low strain rate (Paterson and Wong, 2005).
3. the sample was shattered in multiple small fragments, smaller than the initial grain size of about 1.5 mm. This diffuse damage is reminiscent of pulverized rocks.

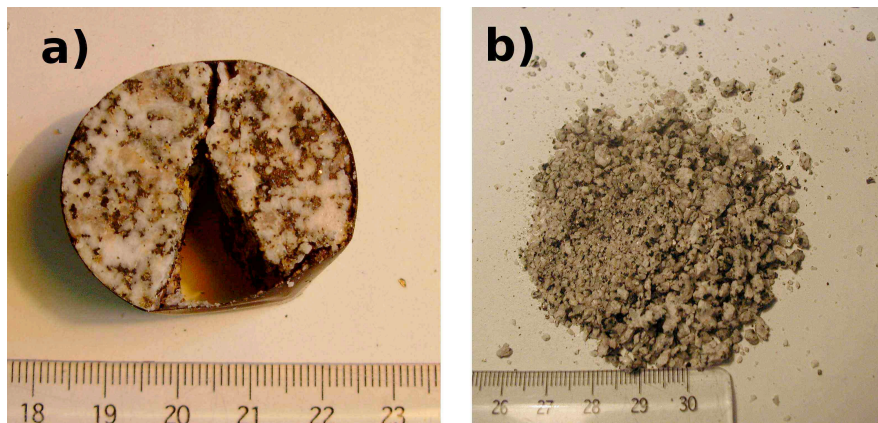


Figure 2.3: (a-left) At a low strain rate (here, 140/s), a granodiorite sample split into a few fragments when deformed in the Split Hopkinson Pressure Bar apparatus. (b-right) At a higher strain rate (here, 400/s), the sample was pulverized into numerous fragments with diameter smaller than the rock initial grain size. The ruler has centimetric marks. From Doan and Gary (2009)

We made other experiments on the Tarn granite, which we used as a proxy for undamaged rocks, and found again only these 3 states. Other authors working independently on Westerly granite found a similar results (Yuan et al., 2011).

No, for limestone

We also tried to reproduce pulverization on carbonate rocks (Doan and Billi, 2011), motivated by the observation of both pulverized granitic rocks and intact limestone on the same outcrop near Lake Hughes.

Contrary to the crystalline rocks, we do think we achieve to get pulverization. First, the final grains do not have a round shape, but a elongated needle-like shape not seen in the . Second,

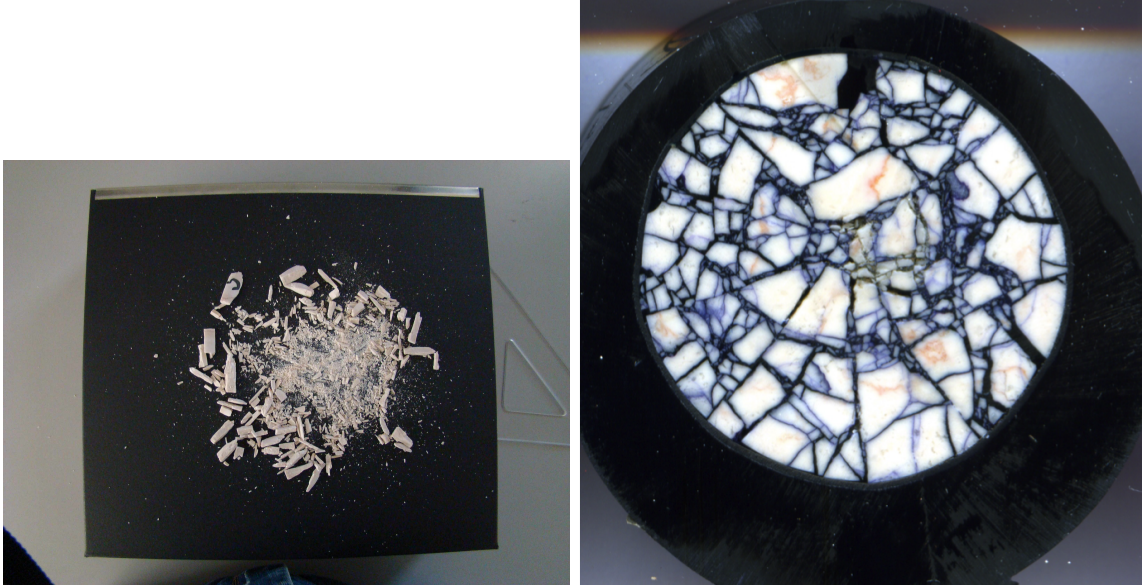


Figure 2.4: Cross-section from a "pulverized" marble sample (Sample B). Diameter is about 2.5 cm. There is a hierarchical fracture pattern, suggesting that deformation localized and the dense microfractured structure results from cumulated faults. On theunjacketed samples, the fragments have a needle shape pattern, suggesting that deformation occurs by accumulating tensile fractures perpendicular to the loading direction.

2.1.2 What are the conditions for pulverizing rocks ?

Macroscopic failure

Several parameters affect the macroscopic failure state. The first one is the strain experienced by the sample, the second one is the strain rate.

The intense fragmentation tends to happen at high strain rate loading. Figure 2.5 summarizes all the tests made on the San Andreas Fault samples (*Doan and Gary, 2009*). Pulverization is achieved if strain rate exceeds a given threshold, here 150 /s. This result is comforted by other studies. For instance, we conducted a similar series of experiments on Tarn granite (*Doan and D'Hour, 2012*), a non pre-damaged rock, for which the scatter of data due to variability is reduced. Similarly, *Yuan et al. (2011)* found also a threshold in pulverization on Westerly granite samples. In these two studies done on intact granitic rocks, the threshold in strain rate is also about 250 /s.

At higher strain, fracture density tends to be larger and could be confused with pulverization. However, structural analysis shows an example from .

We conclude that pulverization may be marker of intense high strain rate damage, certainly above a threshold exceeding 100 /s. Such strain rate is not expected for a standard sub-sonic rupture propagating at a speed below the S wave velocity of the medium. Several hypotheses can be proposed to explain such high strain rate: supershear rupture (*Doan and Gary, 2009*), bimaterial interface (*Shi and Ben-Zion, 2006*) or local heterogeneities that accumulated energy and suddenly fail (*Dunham et al., 2003*). In all cases, pulverized rocks may be records of high frequency shaking, and it may be useful for paleoseismology.

Microscopic failure

Macroscopic description of damage is a convenient way to assess damage patterns, but it lacks quantitative description. To get describable states of damage, the samples were jacketed by a .

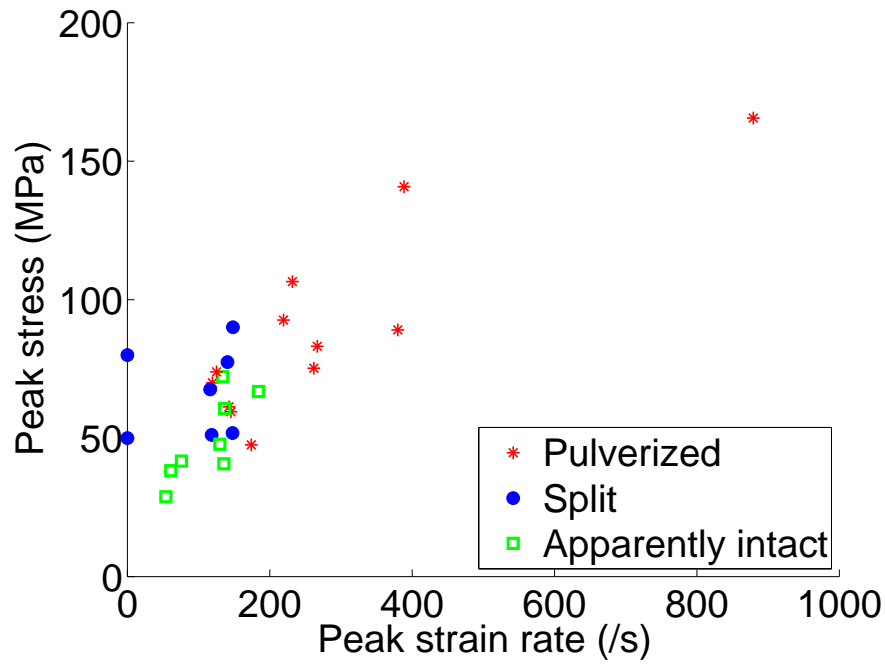


Figure 2.5: Summary of the high strain rate experiments conducted on the samples from the San Andreas Fault. We report the final state of the sample, as a function of the maximum stress reach and the maximum strain rate experienced during the loading.

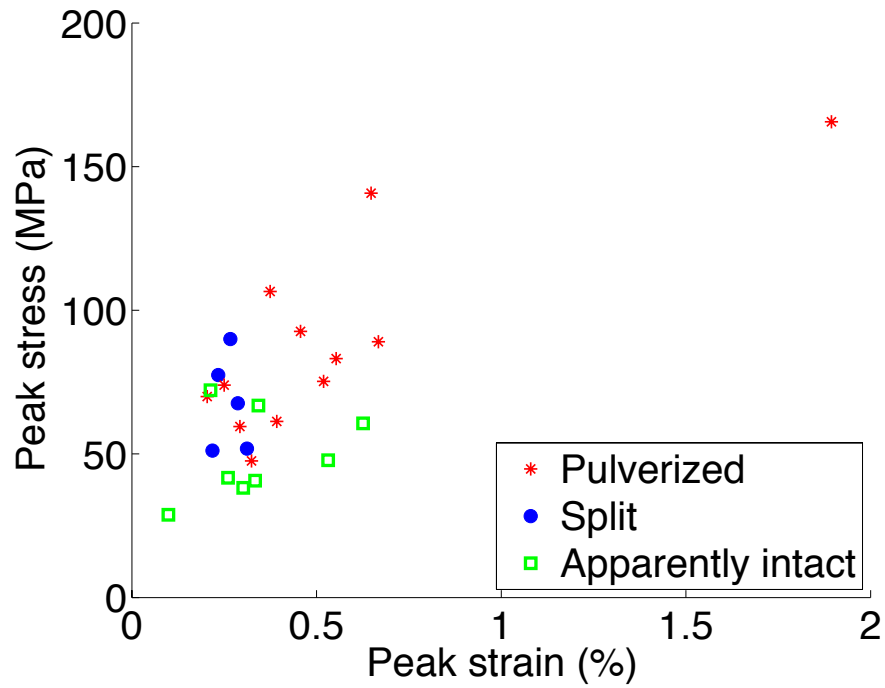


Figure 2.6: Summary of the strain reached for the same experiments as in figure 2.5.

2.2 What are the properties of pulverized rocks?

2.3 Perspectives: Dynamic damage near an active fault

- Quantification of damage through BET measurement of surface area. This study is performed in cooperation with Mike Heap, to investigate
- Reset of thermoluminescence data.

Chapter 3

Variation of hydraulic properties across active faults

Permeability is strongly scale dependent. It is also pressure-dependent. Hence in-situ measurements are key to identify the actual permeability structure near active faults.

Two kinds of measurements are possible: - Direct permeability measurement, through pumping test. The investigated measure depends on the duration and flow rate of the pumping test. Such tests were performed with the MDT tool of IODP expedition 319. - Indirect permeability measurement through geophysical logs. We use datasets of IODP 319 to compare with permeability measurements made with MDT. The technique can also be used a posteriori on datasets from SAFOD.

Chapter 4

Localization process at the onset of coseismic slip

Appendix A

Rock pulverization at high strain rate
near the San Andreas fault / Nature
Geosciences, 2009

Rock pulverization at high strain rate near the San Andreas fault

Mai-Linh Doan^{1*} and Gérard Gary²

In the damage zone around faults, strain is usually localized along fractures, whereas the blocks enclosed by the fractures remain relatively undamaged^{1,2}. Some rocks near the San Andreas fault, however, are pervasively pulverized at distances of up to 400 m from the fault's core³; intense fragmentation at such distances is rarely observed along other fault zones. Moreover, these rocks preserve their original grain shapes, indicating that they experienced low total strain³. Here we use laboratory experiments to show that the intense fragmentation of intact rocks sampled near the San Andreas fault requires high rates of strain ($>150\text{ s}^{-1}$). Our calculations suggest that the combination of the low amount of strain experienced by the pulverized rocks and the high rates of strain indicated by our experiments could be explained by a supershear rupture—a rupture that propagated along the fault at a velocity equal to or greater than that of seismic shear waves.

Northeast of Los Angeles, the Mojave segment of the San Andreas fault shows unusual fault damage. Outcrops have patches of rock finely broken to a scale smaller than the initial grain size of about 1.5 mm; the damage pattern affects mainly crystalline rock that is not extensively weathered, and has only minor clay content^{4,5}. Whereas grain comminution and gouge formation are common within the fault core, where much of the strain occurs, intense pulverization so far from the fault core is unexpected. Here we investigate the role of dynamic loading on the pulverization of rocks near the San Andreas fault by carrying out laboratory experiments on rocks sampled near the fault. We then discuss the implications of these results for the physics of earthquakes.

Dynamic pulverization is a process in which stress localization is inhibited, so that the entire medium can be finely fractured⁶. Strain localization is the consequence of an unstable feedback: the largest pre-existing crack within the material is the most favourable for further fracture propagation, and once extended, it becomes even more amenable to further propagation. As a result, this crack extends at the expense of the others. However, at higher loading rates, this localization process may be inhibited. The favoured crack propagates at a finite rate, limited by the P-wave speed of the medium, and cannot accommodate all of the energy provided to the medium. Other fractures can propagate simultaneously and coalesce to produce numerous small fragments. The sample eventually becomes pulverized⁶.

Dynamic pulverization has already been considered along faults⁷. However, the theory of Reches and Dewers⁷ results in high strain rates for gouge in the fault core, but in much smaller strain rates at several tens of metres away from the core (see Supplementary Discussion). To understand the effect of strain rate on the damage mode, we conducted experiments aimed at understanding the effect of high strain rates on the fragmentation of intact rocks sampled near the pulverized zone of the San Andreas

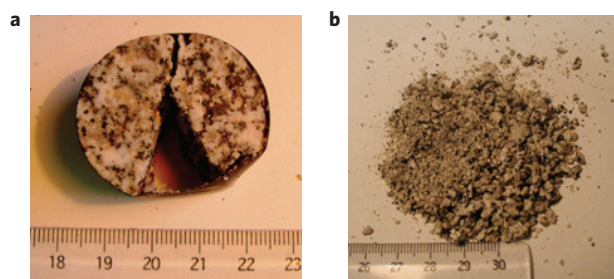


Figure 1 | States of the samples after the experiments. a, At a low strain rate (here, 140 s^{-1}), a rock sample splits into a few fragments when deformed in the SHPB apparatus. **b**, At a higher strain rate (here, 400 s^{-1}), the sample was pulverized into numerous fragments with a diameter smaller than the rock initial grain size. The rulers show centimetres.

fault (Supplementary Figs S5 and S6). The experiments were carried out using a split Hopkinson pressure bar (SHPB) apparatus⁸ in the Laboratoire de Mécanique des Solides of the École Polytechnique, Palaiseau, France. This technique⁹ gives average stress, strain and strain rate in the sample for strain rates as large as $2,000\text{ s}^{-1}$. Details are given in the Methods section.

Experimental results yielded three types of final state (Figs 1 and 2): (1) an unbroken state, where insufficient loading did not allow the sample to break; (2) a simple fracturing state, where a sample was split by a few (at most three) longitudinal fractures—a common damage pattern for uniaxial loading at low strain rate; and (3) a multiple fragmentation state, when the sample was broken into multiple fragments, some with a size smaller than 1 mm. The experiments carried out at a strain rate higher than 150 s^{-1} produced finely broken samples, whereas those carried out below 100 s^{-1} gave samples broken into two or three fragments (Fig. 2). The interval of strain rate (100 s^{-1} – 150 s^{-1}) delimits a transition zone between fracturing and pulverization. In this interval, the maximum stress varies from 50 to 100 MPa, with no clear jump.

We now discuss the pertinence of the laboratory results to explain the natural pulverization. As the tested samples were collected in the damage zone of the San Andreas fault, their Young's modulus is small ($10 \pm 3\text{ GPa}$, about one fifth of the tabulated value for granite¹⁰). The static strength of the material ranges between 50 and 90 MPa, about half the tabulated values for intact granite¹¹. These low values suggest that the initial samples were already damaged. This is confirmed by microstructural studies (see the Methods section and Supplementary Figs S7 and S8). All of these cracks competed with the most favourable crack and helped to prevent strain localization along a single fracture. Consequently, we estimate that our threshold strain rate is a minimum value for the transition to fine fragmentation in the field. To verify

¹Laboratoire de Géophysique Interne et Tectonophysique—CNRS—OSUG, Université Joseph Fourier Grenoble I, BP 53, F-38041 Grenoble, France,

²Laboratoire de Mécanique des Solides, Ecole Polytechnique, F-91128 Palaiseau, France. *e-mail: Mai-Linh.Doan@obs.ujf-grenoble.fr.

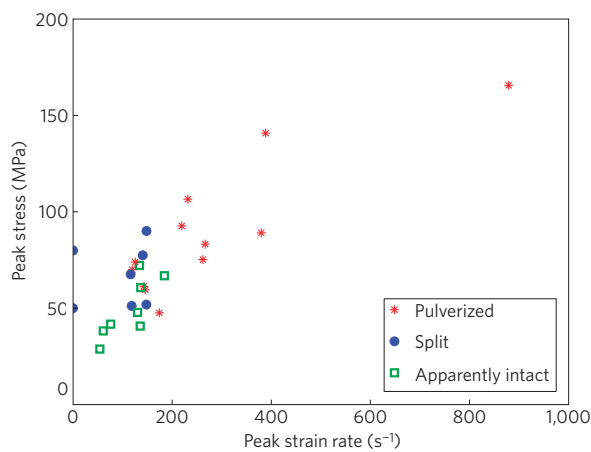


Figure 2 | Experimental results. The final state relative to the peak stress and the peak strain rate. The transition from single crack fracture (blue circles; Fig. 1a) to intense pulverization (red stars; Fig. 1b) depends on strain rate. The threshold occurs between 100 s^{-1} and 150 s^{-1} . Some samples remained unbroken (green squares).

the dependence of our results on the initial damage state, we carried out similar experiments on intact granite samples from Tarn, France (Supplementary Figs S9 and S10). We found a similar transition from sparse fracturing to fragmentation, but at a higher strain rate, about 250 s^{-1} . The fragmentation happens during the first loading (Fig. 3).

Our transition not only delimits different final damage patterns, but also corresponds to an increase in the apparent strength of the sample. These experimental results are in accordance with the statistical theory of Hild¹² for the transition from single to multiple fracturing regimes. In both theory and experiment, rock strength starts to increase with strain rate, once in a pulverization regime. Theoretically, there is an intrinsic increase of the material strength¹³, because the propagation of several small fractures requires more energy than that of a single large fracture. Experimentally, the sample does not instantaneously expand laterally at high strain rates, and hence is dynamically confined. When computing the equivalent constraining stress¹⁰, we retrieve dynamic confining pressures in the range of 2–10 MPa, corresponding to a burial depth of only 80–400 m. This suggests that pulverization may also be found in the shallow subsurface, as confirmed by borehole studies¹⁴.

Grain size analyses were carried out on fractured and pulverized rocks (see the Methods section and Supplementary Tables S2 and S3). Most particles have millimetric dimensions, a little larger than the grain size of pulverized rocks⁵. We do not claim to reproduce the exact state of pulverized rocks, especially its grain size distribution. The natural state is certainly the result of several earthquakes, each one damaging rocks by compressional and shear loading waves. Here, we focus only on the transition between localized fracturing and pervasive fragmentation.

We focused on dynamic pulverization to explain pulverization near faults. Other mechanisms may inhibit the strain localization process. One is the ductile–fragile transition at high confining stress or high temperature¹⁵. However, both parameters are below the transition values (300 MPa, $350 \text{ }^\circ\text{C}$; ref. 15) for crystalline rocks at the ground surface. A second way to inhibit strain localization is to apply fast rotating stress. The sheared zones are then reworked over and over, so that the strain localization is annealed at the expense of the formation of preferential microstructure orientation¹⁶. This mechanism requires large strain, which is not observed in the pulverized rocks from the San Andreas fault because they preserve their original fabric.

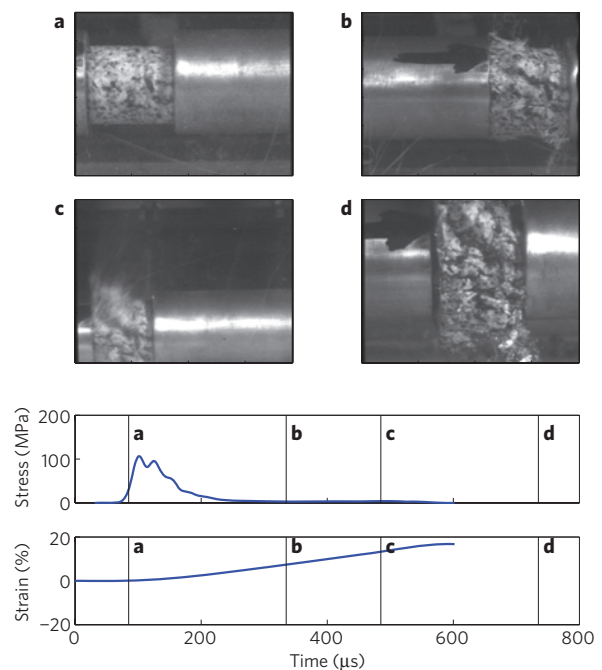


Figure 3 | Time-lapse snapshots of a sample being pulverized. The vertical bars **a–d** in the plots at the bottom denote the times corresponding to the photographs, taken with four independently triggered cameras. The measured stress and strain history is reported in the lower graphs. The sample breaks in an early stage (after **a**), but because of their inertia, the fragments fly away later (**b,c,d**). The sample is fragmented while in compression, and not during stress relaxation.

A high strain rate may be a necessary condition for pulverization, although perhaps not a sufficient condition. Other phenomena can also modulate the onset of pulverization. For instance, rupture along an interface separating material with different elastic moduli can induce tensile loading on only one side¹⁷. As tensile strength is small, damage is facilitated there. This may explain the asymmetry of damage along faults.

There are also some caveats in relating the laboratory experiments to the field observations. Our experiments were carried out under uniaxial loading. The transition strain rate depends on the speed of fracture propagation and on the interaction between cracks, which are controlled by the statistics of the initial crack population and the size of stress shadow zones around each crack. These parameters do not strongly depend on the fracture mode¹⁸. The fracture speed propagation is close to the S-wave speed c_s in all fracture modes. The shape of the stressed areas around a crack tip differs with fracture mode, but its size varies similarly, with stress decaying with distance from the fracture tip r as $1/r^{1/2}$. Hence, the transition from single to multiple fracturing is only weakly dependent on the fracture mode¹⁸. The strain rate condition obtained experimentally is a reasonable approximation to the natural case in that the sample is subject to both shear stress and normal stress.

Figure 2 suggests that the transition from fracturing to pulverization is related to strain rate. An important result of this study is that pulverized rocks appear as markers of high strain rate loading ($> 150 \text{ s}^{-1}$). This result needs to be evaluated in light of the fact that the initial structure of the pulverized rocks found in the field is preserved, which suggests that the pulverized rocks endured low strain.

To determine the conditions that are required to satisfy the twin constraints of high strain rate but low strain, we computed the strain rate and the stress near a crack tip propagating at a constant velocity. Considering distances from the fault ($r = 100 \text{ m}$) that are small relative to the rupture size (more than 10 km), we calculate

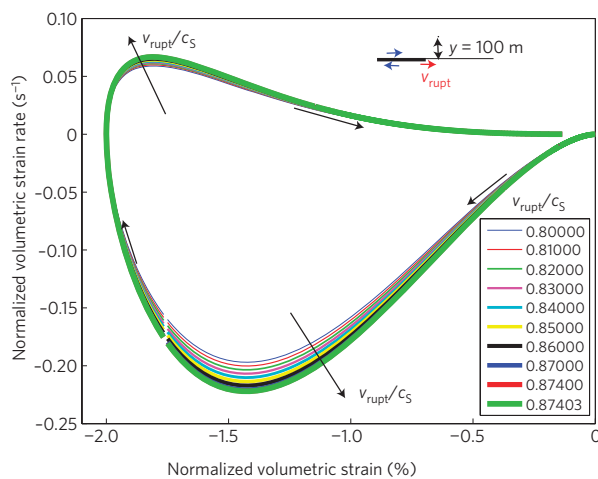


Figure 4 | Dilatational strain rate versus dilatational strain induced by a subshear rupture 100 m from the fault core. We normalized both the strain and strain rate so that the maximum strain amplitude is 2%, corresponding to the order of magnitude of the maximum strain in the pulverized rocks near the San Andreas fault. The curves were computed in plane stress for several rupture speeds, all below the Rayleigh wave speed (here $c_R \sim 0.874030c_S$). All curves achieve a maximum strain rate less than 0.25 s^{-1} , three orders of magnitude below our experimental 150 s^{-1} pulverization threshold.

an asymptotic development of stress, dependent on the distance to the rupture tip (see Supplementary Discussion for details of the calculations). The first terms of strain and strain rate for a rupture speed below the S-wave speed (subshear rupture) decay as $1/r^{1/2}$ and $1/r^{3/2}$, respectively¹⁹. Figure 4 gives the shear strain rate of rocks located 100 m from the fault supposing that the maximum strain is 2%, a value we believe is representative of the maximum strain sustained by the pulverized rocks. The maximum strain rate remains two orders of magnitude below the experimental threshold strain rate permitting pulverization. Other terms of the Taylor expansion of strain²⁰ give similar or lower strain rates for strains less than 2%. Attaining the experimental threshold is therefore unlikely for subshear rupture in homogeneous material.

In the previous calculation, we made two hypotheses: a homogeneous medium and a subshear rupture. For faults separating two different media, a sharp tensile pulse can be generated in the stiffest part of the fault^{21,22}. If the Weertman pulse induces pulverization, we expect to find pulverized rocks along faults separating different materials, with no evidence for compression. However, pulverized sandstone along the San Andreas fault shows compression features²³. Pulverized rocks are sometimes found on both sides of the San Andreas fault³. Hence, we propose that an alternative mechanism, supershear rupture, generates the high strain rate and pulverizes rocks.

Supershear rupture induces a shock wave. Simple models yield Heaviside functions, modelling sharp fronts and with small decay with distance¹⁹ (see Supplementary Discussion for details). High rates of loading can be reached 100 m from the fault core, as supershear rupture induces a shock wave²⁴ and generates high-frequency displacements²⁵. This is consistent with the discovery of pulverized rocks only near large strike-slip faults: San Andreas and San Jacinto faults in California^{3,5,23}, Northern Anatolia fault in Turkey²⁶, Arima-Takatsuki fault in Japan²⁷, which are the most amenable to supershear rupture. We predict that off-fault pulverization should only be found along large strike-slip faults, and this provides a way to test our hypothesis in the future.

This work offers constraints on the formation of pulverized rocks, which endured deformation rates higher than 150 s^{-1} .

As possible indicators of previous supershear rupture, and independent of seismological observations, pulverized rocks should therefore be considered in the risk assessment of such potentially damaging earthquakes.

Methods

We experimentally damaged rocks sampled near the pulverized zone at high strain rate, using an SHPB apparatus⁸ in the Laboratoire de Mécanique des Solides of the École Polytechnique, Palaiseau, France.

Samples. Samples were collected about 200 m away from the fault core, in the Lake Hughes area (see Supplementary Fig. S5). The rocks were strong enough to be cored. We used this rock material to approximate pulverized rocks as it was before pulverization: the same material, not yet pulverized, but still damaged, as they lay near an active fault.

The samples were taken as boulders in the flanks of a deep gully. As they lay above the bottom of the gully, we assume the boulders were not transported by water, but rather that they fell by gravity from the edges of the gully. The flanks are quite steep, so that the originating outcrops could not be investigated.

Thin sections of the samples (Supplementary Figs S7 and S8) show alteration and dense microfracturing. Hence, we also used samples of Tarn granite, as a supplementary testing. Thin sections in Supplementary Fig. S8 show that the granite is slightly altered but less fractured than the samples from the San Andreas fault.

Experimental device. The experiments were carried out using the device shown in Supplementary Fig. S2. Each sample is inserted between two bars and impacted by a 'striker' arriving with a known speed. The incident stress wave splits into reflected and transmitted waves when it reaches the sample. Incident and reflected waves are measured with a strain gauge on the input bar, and the transmitted wave with a strain gauge on the output bar. Subsequent waves are not recorded as they are superposed at gauge locations and cannot be easily identified.

Processing. Classical processing of the SHPB supposes one-dimensional (1D) propagation of an elastic wave, given the dimensions of the bars (3 m long and 4 cm diameter). Here, we use a very precise measurement of time (with modern data acquisition systems) and a very precise 3D modelling of the wave propagation in bars (based on the Pochhammer and Chree equations) for the computation of forces and displacements at both ends of the specimen. We checked that the forces were identical at the input and output bars, to verify that the sample was homogeneously loaded. Once the quasi-equilibrium of the specimen was verified (equality of input and output forces), we calculated stress, strain and strain rate. A direct measurement of Young's modulus of the specimen is also possible, based on the transient 1D analysis of the test.

Grain size distribution. Some samples were wrapped inside a loose plastic bag attached to the input and output bars of the SHPB apparatus. This allowed us to limit the loss of material during the pulverization of the sample and to conduct grain size analysis (see Supplementary Tables S2 and S3). The grain size distribution of the larger grains was determined by manual sieving by shaking a stack of sieves for 2 min.

Errors in grain size distribution are mainly due to loss of material, which is about 1 g for an initial sample of 25 g. This is also the range of weights measured for each sieve. Hence, the weight of each particle size bin may be underestimated by 100%. Theoretically, all size bins are affected. However, fragmentation experiments produce a large dust cloud that could not be recovered. The contributions of the smallest particles were almost certainly the most underestimated.

Sieving methods measure weight and are biased towards the largest particles, because weight scales as the cube of the particle size. It is therefore difficult to make a quantitative comparison with the natural grain size distribution obtained with a laser granulometer that counts particle number⁵. Still, qualitatively, our grain size is larger than the natural grain size distribution of pulverized rocks, but smaller than the original grain size of our samples.⁷

Modal analysis. We carried out modal analysis of two thin sections drilled within a sample taken near Lake Hughes outcrop (see Supplementary Fig. S5), and one thin section drilled within a sample of Tarn granite. The modal analysis of each thin section was conducted by identifying the mineral located at 315 random points within the thin section. The error estimation can be quantified using the central limit theorem²⁸. If a mineral is found n times for N point counts, the upper limit of the 95% confidence interval is computed as

$$P^u = 100 * \beta(1 - \alpha, n + 1, N - n)$$

where $\alpha = 1 - 0.95$ and β is the inverse of the beta cumulative distribution function. The lower bound of the 95% confidence interval is computed as

$$P_l = 100 * [1 - \beta(1 - \alpha, N - n + 1, n)]$$

Received 18 February 2009; accepted 27 August 2009;
published online 27 September 2009

References

- Caine, J. S., Evans, J. P. & Forster, C. B. Fault zone architecture and permeability structure. *Geology* **24**, 1025–1028 (1996).
- Chester, F. M., Evans, J. P. & Biegel, R. L. Internal structure and weakening mechanisms of the San Andreas fault. *J. Geophys. Res.* **98**, 771–786 (1993).
- Dor, O., Ben-Zion, Y., Rockwell, T. K. & Brune, J. N. Pulverized rocks in the Mojave section of the San Andreas fault zone. *Earth Planet. Sci. Lett.* **245**, 642–654 (2006).
- Wilson, B., Dewers, T., Reches, Z. & Brune, J. Particle size and energetics of gouge from earthquake rupture zones. *Nature* **434**, 749–752 (2005).
- Rockwell, T. K. *et al.* Granulometric and mineralogical properties of pulverized rocks from Tejon Pass on the San Andreas fault and from Tejon Ranch on the Garlock fault, California. *Pure Appl. Geophys.* (in the press).
- Grady, D. E. & Kipp, M. E. in *Fracture Mechanics of Rocks* (ed. Atkinson, B. E.) (Academic, 1989).
- Reches, Z. & Dewers, T. A. Gouge formation by dynamic pulverization during earthquake rupture. *Earth. Planet. Sci. Lett.* **235**, 361–374 (2005).
- Kolsky, H. *Stress Waves in Solids* (Dover Publications, 1963).
- Zhao, H. & Gary, G. On the use of SHPB techniques to determine the dynamic behavior of materials in the range of small strains. *Int. J. Solids Struct.* **33**, 3363–3375 (1996).
- Forrestal, M. J., Wright, T. W. & Chen, W. The effect of radial inertia on brittle samples during the split Hopkinson pressure bar test. *Int. J. Impact Eng.* **34**, 405–411 (2007).
- Lide, D. R. (ed.) in *CRC Handbook of Chemistry and Physics: A Ready-Reference Book of Chemical and Physical Data* 88th edn (Boca Raton, 2008).
- Hild, F., Forquin, P. & Cordeiro da Silva, A. R. Single and multiple fragmentation of brittle geomaterials. *Rev. Franco. Gen. Civ.* **7**, 973–1003 (2003).
- Li, Q. M. & Meng, H. About the dynamic strength enhancement of concrete-like materials in a split Hopkinson pressure bar test. *Int. J. Solids Struct.* **40**, 343–360 (2003).
- Wechsler, N., Allen, E. E., Rockwell, T. K., Chester, J. & Ben-Zion, Y. Characterization of pulverized granite from a traverse and a shallow drill along the San Andreas fault, Little Rock, CA. *Seismological Society of America Annual Meeting, Seismol. Res. Lett.* **80**, 319 (2009).
- Guéguen, Y. & Palciauskas, V. *Introduction to the Physics of Rocks* (Princeton Univ. Press, 1994).
- Bystricky, M., Kunze, K., Burlini, L. & Burg, J. P. High shear strain of olivine aggregate: Rheological and seismic consequences. *Science* **290**, 1564–1567 (2000).
- Ben Zion, Y. & Andrews, D. J. Properties and implication of dynamic rupture along a material interface. *Bull. Seismol. Soc. Am.* **88**, 1084–1094 (1998).
- Huang, C., Subhash, G. & Vitton, S. J. A dynamic damage growth model for uniaxial compressive response of rock aggregates. *Mech. Mater.* **34**, 267–277 (2002).
- Freund, L. B. *Dynamic Fracture Mechanics* (Cambridge Univ. Press, 1990).
- Xu, Y. & Keer, L. M. Higher order asymptotic field at the moving crack tip. *Int. J. Fracture* **58**, 325–343 (1992).
- Ben-Zion, Y. Dynamic ruptures in recent models of earthquake faults. *J. Mech. Phys. Solids* **49**, 2209–2244 (2001).
- Andrews, D. J. & Ben-Zion, Y. Wrinkle-like slip pulse on a fault between different materials. *J. Geophys. Res.* **102**, 553–571 (1997).
- Dor, O., Chester, J. S., Ben-Zion, Y., Brune, J. N. & Rockwell, T. K. Characterization of damage in sandstones along the Mojave section of the San Andreas Fault: Implications for the shallow extent of damage generation. *Pure Appl. Geophys.* **166**, doi:10.1007/s00024-009-0516-z (2009).
- Rosakis, A., Samudrala, O. & Coker, D. Cracks faster than the shear wave speed. *Science* **284**, 1337–1340 (1999).
- Bizarri, A. & Spudich, P. Effects of supershear rupture speed on the high-frequency content of S waves investigated using spontaneous dynamic rupture models and isochrone theory. *J. Geophys. Res.* **113**, B05304 (2008).
- Dor, O. *et al.* Geological and geomorphologic asymmetry across the rupture zones of the 1943 and 1944 earthquakes on the North Anatolian fault: Possible signals for preferred earthquake propagation direction. *Geophys. J. Int.* **173**, 483–504 (2008).
- Mitchell, T. M., Shimamoto, T. & Ben-Zion, Y. Pulverized fault rocks along the Arima-Takatsuki Tectonic line, Japan: Fault structure, damage distribution and textural characteristics. *EGU General Assembly, Geophys. Res. Abstr.* **11**, EGU2009-11751-2 (2009).
- Howarth, R. J. Improved estimators of uncertainty in proportions, point-counting, and pass-fail test results. *Am. J. Sci.* **298**, 594–607 (1998).

Acknowledgements

We thank R. Barre, C. Rousseau, J.-B. Toni, R. Leau and R. Guiguet for their technical help and F. Hild, K. Safa, M. Bouchon and P. Favreau for discussions on this paper; V. D'Hour made preliminary work on Tarn granite. We thank E. Brodsky, F. Renard, J.-P. Gratier, Y. Ben-Zion, S. Boutareaud, P. Molnar and R. Hellmann for reading previous drafts of this manuscript. This work was financially supported by the 3F INSU/CNRS program and by the PPF 'Systèmes Complexes' of the University Joseph Fourier.

Author contributions

M.L.D. proposed and participated in the experiments, processed the data and made the computations. M.L.D. also made the grain size distribution measurements and modal analysis. G.G. developed the SHPB apparatus at the École Polytechnique and was in charge of the experiments.

Additional information

Supplementary information accompanies this paper on www.nature.com/naturegeoscience. Reprints and permissions information is available online at <http://npg.nature.com/reprintsandpermissions>. Correspondence and requests for materials should be addressed to M.L.D.

Appendix B

High strain rate damage of Carrara
marble / Geophysical Research Letters,
2011

High strain rate damage of Carrara marble

Mai-Linh Doan¹ and Andrea Billi²

Received 4 August 2011; revised 2 September 2011; accepted 2 September 2011; published 8 October 2011.

[1] Several cases of rock pulverization have been observed along major active faults in granite and other crystalline rocks. They have been interpreted as due to coseismic pervasive microfracturing. In contrast, little is known about pulverization in carbonates. With the aim of understanding carbonate pulverization, we investigate the high strain rate (c. 100 s^{-1}) behavior of unconfined Carrara marble through a set of experiments with a Split Hopkinson Pressure Bar. Three final states were observed: (1) at low strain, the sample is kept intact, without apparent macrofractures; (2) failure is localized along a few fractures once stress is larger than 100 MPa, corresponding to a strain of 0.65%; (3) above 1.3% strain, the sample is pulverized. Contrary to granite, the transition to pulverization is controlled by strain rather than strain rate. Yet, at low strain rate, a sample from the same marble displayed only a few fractures. This suggests that the experiments were done above the strain rate transition to pulverization. Marble seems easier to pulverize than granite. This creates a paradox: finely pulverized rocks should be prevalent along any high strain zone near faults through carbonates, but this is not what is observed. A few alternatives are proposed to solve this paradox. **Citation:** Doan, M.-L., and A. Billi (2011), High strain rate damage of Carrara marble, *Geophys. Res. Lett.*, 38, L19302, doi:10.1029/2011GL049169.

1. Introduction

[2] Pulverized rocks have been recently identified near some major active faults [Dor *et al.*, 2006, 2009; Mitchell *et al.*, 2011] as a rare example of fault damage, where intense microfracturing occurred while the primary rock structure experienced a minimal distortion (i.e., no or minimal shear strain). Intense damage occurred at low shear strain and microfractures permeated the whole rock using original grain boundaries or crosscutting them, thus producing a very fine-grained material with most grains smaller than 1 mm.

[3] The origin of pulverized rocks is still debated. Their occurrence along major faults suggests a connection with fault mechanics and, in fact, experimental data suggest that pulverization is a marker of coseismic damage due to strong earthquakes [Doan and Gary, 2009]. Pulverized rocks may thus provide important clues to advance the understanding of earthquake physics and seismic faults [Reches and Dewers, 2005; Wilson *et al.*, 2005; Dor *et al.*, 2006; Yuan *et al.*, 2011].

[4] The knowledge of natural pulverized rocks is, however, still very limited under many aspects. For instance, known occurrences of pulverized rocks are so far limited to only a

few sites and major faults (all strike-slip, with prominent bimaterial interfaces), namely along the San Andreas Fault system [Wilson *et al.*, 2005; Dor *et al.*, 2006; Rockwell *et al.*, 2009; Wechsler *et al.*, 2011], the Northern Anatolian Fault [Dor *et al.*, 2008], and the Arima-Takatsuki Fault [Mitchell *et al.*, 2011]. Interestingly, occurrence of pulverization is so far limited to a small number of lithologies, mainly crystalline rocks, with the exception of a sandstone outcrop along the San Andreas Fault [Dor *et al.*, 2009].

[5] In carbonate rocks, finely-comminuted fault rocks with grains smaller than 1 mm occur in high shear strain zones (i.e., the fault core [e.g., Storti *et al.*, 2003; Billi and Storti, 2004; Billi, 2005; Agosta and Aydin, 2006; Frost *et al.*, 2009]). In contrast, low-strain, poorly-distorted, fault-related breccias are relatively common, but always in low-strain zones (i.e., the damage zone) and usually with large grains (>1 cm) [Billi *et al.*, 2003], much larger than for the usual pulverized rocks (<1 mm). So far, the only exception is the carbonate fault rock observed in central Italy along a seismically-active normal fault cutting through shallow-water Mesozoic limestone, where finely comminuted rock (grains up to c. 1 cm in maximum size), interpreted as pulverized rock for the occurrence of apparently preserved layering, forms a 1-m-thick band running along the fault core on the footwall side [Agosta and Aydin, 2006]. The hangingwall is downthrown and buried so no information is available about a possible bimaterial interface effect. Moreover, the true origin of this rock (i.e., the pulverized limestone) has still to be conclusively ascertained by microscopic observations. Other reported cases of preserved carbonate rocks embedded within pulverized crystalline rocks [see Dor *et al.*, 2006, Figure 5] suggest a scarce propensity of carbonates to pulverization.

[6] To understand why carbonates seem so little prone to pulverization, we ran high strain rate testing of carbonate rocks in the laboratory. As sedimentary carbonates are very heterogeneous, we focused our first study of carbonate dynamic pulverization on the most homogeneous and crystalline variety of carbonate (i.e., the Carrara marble; Figure 1a). Dynamic loading was done with a Split Hopkinson Pressure Bar apparatus [Chen and Song, 2010] to record the uniaxial behavior of samples at strain rates on the order of 100 s^{-1} .

[7] After presenting the experimental method, we relate the evolution of strength and damage pattern to strain and strain rate. We discuss the experimental results in light of the microstructural damage, before concluding on the relevance of our study to seismic faults in carbonates.

2. Method

[8] Experiments were done using a Split Hopkinson Pressure Bar (SHPB) apparatus in the Laboratoire de Mécanique des Solides of the École Polytechnique, Palaiseau, France. Each sample was inserted between two bars impacted by a

¹Institut des Sciences de la Terre, Université Joseph Fourier, Grenoble, France.

²IGAG, Consiglio Nazionale delle Ricerche, Rome, Italy.

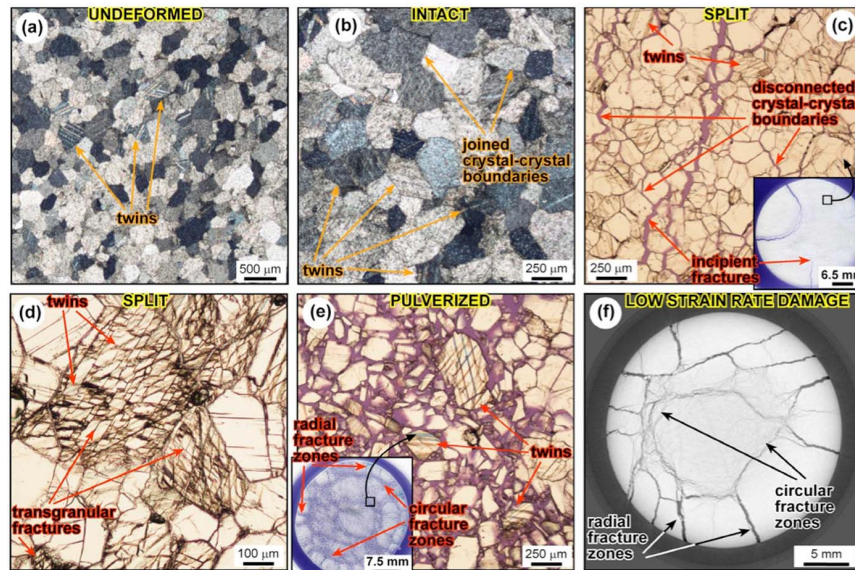


Figure 1. Microphotographs of Carrara marble samples. Figures 1b–1e are perpendicular to loading in the SHPB apparatus and Figure 1f is perpendicular to loading in the low strain rate apparatus. (a) Undeformed Carrara marble (crossed nicols). Note episodic calcite twinning. (b) Apparently intact sample M04 (crossed nicols). Note calcite twins and joined boundaries between crystals. (c) Split sample M16 (parallel nicols). Note a rather pervasive incipient disarticulation of crystal-crystal boundaries. Inset shows a thin-section parallel and close to the input surface of the cylindrical sample M16. The large microphotograph is taken from the thin-section in the inset. Note the occurrence of incipient radial fractures and incipient disarticulation of crystal-crystal boundaries. At least in places, calcite twinning preceded fracturing as shown by twins cut by fractures. (d) Enlargement from split sample M16 (parallel nicols). Note transgranular fractures cutting through twinned non-distorted grains. (e) Pulverized sample M01 (parallel nicols). Inset shows a thin-section parallel and close to the input surface of the cylindrical sample M01. Note the radial and circular main fracture zones affecting the thin-section. The large microphotograph is taken from the thin-section in the inset and shows a complete disarticulation of the crystal-crystal boundaries plus fractures breaking the original grains, some of which contain calcite twins. (f) Damage pattern of Carrara marble subjected to low strain rate deformation. Note large strain (fractures) occurred under low strain rate.

striker bar arriving at a known velocity. The dimensions of the bars (length: 3 m; diameter: 4 cm) are so that the propagation of elastic waves in the bars is mainly one-dimensional [Gama *et al.*, 2004]. Using the first mode solution of the Pochhammer-Chree equation of wave propagation in bars, forces and displacements applied to the bar ends were retrieved from strain gauges glued on the bars. We checked that the forces were identical at the input and output bars to

ensure that the sample was homogeneously loaded. We could then derive the history of stress, strain, and strain rate experienced by the sample. Due to their short duration, experiments were not servo-controlled. The loading duration is related to the length of the striker bar. Hence, strain tends to increase with strain rate. We compensate for this drawback of the SHPB apparatus by changing the material of the bars and by varying the length of the striker.

Table 1. Summary of Experimental Data

| Sample | Length (mm) | Diameter (mm) | Max. True Stress (MPa) | Max True Strain Rate (s^{-1}) | Max True Strain (%) | Dissipated Volumetric Energy (MJ/m^3) | Rubber Jacket | Post-experiment State ^a |
|--------|-------------|---------------|------------------------|-----------------------------------|---------------------|---|---------------|------------------------------------|
| M01 | 28.06 | 25.62 | 121 | 202 | 3.38 | 2.03 | yes | pulverized (red) |
| M02 | 27.65 | 25.64 | 110 | 209 | 3.64 | 1.88 | yes | pulverized (red) |
| M03 | 28.65 | 25.97 | 103 | 120 | 1.82 | 1.18 | yes | pulverized (red) |
| M04 | 28.75 | 25.59 | 66 | 42 | 0.38 | 0.12 | yes | intact (green) |
| M05 | 28.31 | 25.66 | 101 | 140 | 2.19 | 1.39 | yes | pulverized (red) |
| M07 | 28.64 | 25.61 | 110 | 205 | 3.49 | 1.74 | no | pulverized (red) |
| M08 | 28.27 | 25.67 | 108 | 131 | 1.37 | 1.09 | yes | pulverized (red) |
| M10 | 28.12 | 25.68 | 35 | 16 | 0.15 | 0.02 | yes | intact (green) |
| M12 | 28.19 | 25.58 | 106 | 84 | 0.60 | 0.32 | yes | intact (green) |
| M13 | 28.49 | 25.62 | 99 | 86 | 0.73 | 0.45 | yes | split (blue) |
| M15 | 28.66 | 25.66 | 79 | 116 | 1.86 | 1.05 | no | pulverized (red) |
| M16 | 28.22 | 25.63 | 110 | 91 | 0.98 | 0.74 | no | split (blue) |
| M17 | 28.46 | 25.68 | 127 | 35 | 0.69 | 0.51 | no | split (blue) |
| M18 | 27.74 | 25.69 | 129 | 68 | 1.66 | 1.36 | no | pulverized (red) |

^aColors in parentheses correspond to the classification of final macroscopic damage of Figure 3.

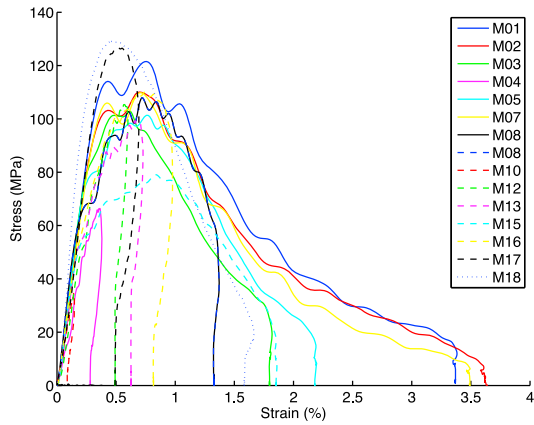


Figure 2. Experimental strain-stress curves of all samples. The peak stress is consistent for all the sample. The Young modulus is also similar, around 10 GPa.

[9] We deformed 14 cylindrical samples (length and diameter: c. 25 mm; Table 1) of Carrara marble. The fine grain size of the Carrara marble (c. 0.2–0.4 mm; Figure 1) is much smaller than the dimension of the sample. Some samples were jacketed with a rubber jacket to preserve and study the post-experiment deformation fabric. We then impregnated these samples with an indurative epoxy resin and cut them to analyze their fabric under an optical microscope (Figure 1).

[10] We also conducted a quasi-static uniaxial compressive test on a jacketed sample using a Schenk press located at the 3SR Laboratory in Grenoble, France, with a strain rate of 10^{-5} s^{-1} only. We used also the X-Ray CT scan tomography of the same laboratory to microstructurally investigate the sample after the quasi-static test (Figure 1f). Details on the

scanning apparatus and processing of data from the X-Ray CT Scan are similar to *Lenoir et al.* [2007].

3. Results

[11] With increasing strain and strain rate, we obtained three main post-experimental deformation fabrics (Table 1): (1) strongly cohesive, apparently intact samples (i.e., apparently intact or with one or two incipient fractures at the most; Figure 1b), (2) poorly cohesive, split samples (i.e., with some main fractures splitting the sample in a few large fragments; Figures 1c and 1d), and (3) uncohesive, pulverized samples (i.e., with diffuse microfractures and most fragments less than 1 mm in size; Figure 1e), where the distance between microfractures is about $500 \mu\text{m}$.

[12] Before failure, the samples experienced similar elastic loading phases (Figure 2), with a Young’s modulus of 20 GPa. The Young’s modulus is not sensitive to strain rate. Strength of the sample is about 100 MPa, similar to the strength recorded in the literature for low strain rate experiments on Carrara marble at room temperature and 5 MPa of confining pressure [*Fredrich et al.*, 1989]. Below the 100 MPa threshold, we do not see any macroscopic diffuse damage (Figures 1 and 3 and Table 1). Note that, in all experiments, there is a permanent strain (Figure 2) suggesting that inelastic processes occurred (e.g., twinning and microfracturing; Figure 1).

[13] Diagrams of strain and strain rate vs. the maximum stress attained in the samples as well as the diagram of strain vs. the energy dissipated in the experiments are shown in Figure 3. These experimental results show that, although an approximate trend toward pulverization with increasing strain rate is visible (see, for instance, results from samples M01, M02, M03, M07, M08, M05, and M15 in Table 1), unlike granite [*Doan and Gary*, 2009; *Yuan et al.*, 2011], in the Carrara marble, the transition between split and pulverized

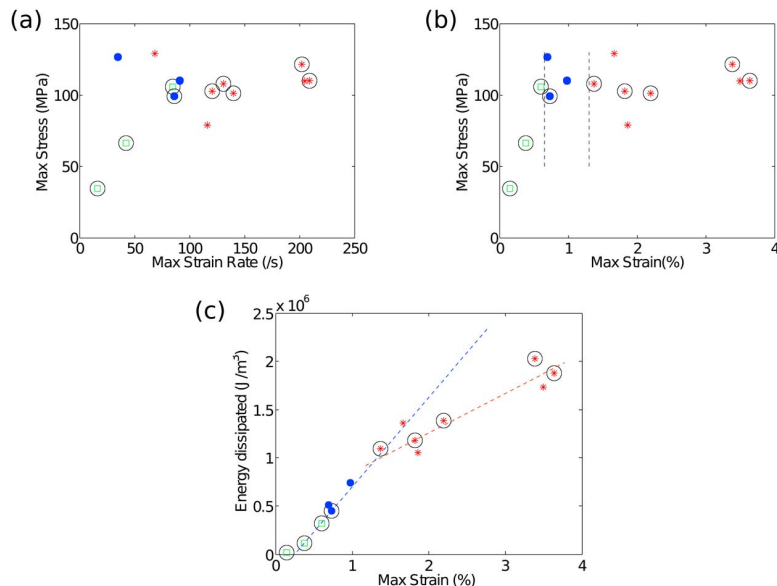


Figure 3. Phase diagrams of the macroscopic damage patterns. (a) Maximum strain rate vs. maximum stress. (b) Maximum strain vs. maximum stress. (c) Dissipated energy vs. maximum stress. Green squares, blue circles, and red asterisks indicate, respectively, apparently intact, split, and pulverized samples. Jacketed samples are indicated with a circle surrounding the damage symbol.

rocks with strain rate is not obvious (Figure 3a). Sample M18, for instance, is pulverized for a strain rate of 68 s^{-1} , whereas sample M13 is simply split by some main macroscopic fractures for a strain rate of 86 s^{-1} (Table 1). In contrast, the post-experiment damage pattern seems well correlated with the total strain accumulated (Figure 3b) rather than strain rate (Figure 3a). Macroscopic fractures appear in split samples when strain exceeds 0.65%, whereas intense microscopic fragmentation (pulverized samples) appears at strains beyond 1.3%. There is, therefore, a narrow interval during which a few macroscopic fractures develop (the interval between vertical dashed lines in Figure 3b). For higher strains, microscopic fractures pervade samples up to their pulverization (strain $> 1.3\%$) by primarily using crystal-crystal boundaries and, more rarely, cutting through crystals (Figure 1). Hence, marble pulverization is primarily controlled by strain rather than strain rate (Figure 3).

[14] In Figure 3, samples that were jacketed are plotted with circled symbols. Their final macroscopic state is the same as the final state of unjacketed samples loaded under the same conditions. Their strain-stress curve is also similar (Figure 2). Hence, jacketing has no effect on the mechanical results (Figure 3). We can safely analyze the sample microstructure and generalize to the whole dataset. The pertinence of our experimental results to explain the natural pulverization of carbonates is discussed in the following sections.

4. Damage Processes

[15] Carbonate rocks display both ductile and brittle behavior even at low confining pressure [Evans and Kohlstedt, 1995]. In our samples, calcite twinning (crystal-plastic deformation) is very moderate even in finely pulverized samples (Figure 1e). Moreover, limited twinning is present also in the undeformed marble (Figure 1a). Hence, plastic energy by twinning is not the main damage process and energy sink in our high strain rate experiments, where, in contrast, fractures play a major role in damage formation (Figure 1) and are most likely the main energy sink.

[16] In the apparently intact samples, the crystal-crystal boundaries appear (under the optical microscope) tightly joined (Figure 1b). In contrast, the same boundaries start to be diffusively disconnected in the split samples (Figure 1c) and become totally disconnected in the pulverized samples, where crystals are split apart from each other, and, in places, transgranular fractures split the original crystals into multiple subgrains (Figure 1e). In some cases, twinning predates fracturing (Figure 1c), whereas in other cases, fractures occur without shearing the pre-existing twins (Figure 1d).

[17] Without confining pressure, the sample splits naturally into several radial fractures. Figure 1c shows that the incipient fractures are radial fractures nucleated from the sample edge, a free surface where the inertial confinement effects [Forrestal et al., 2004] are small. Tensional strength of rock is smaller than the compressional strength [Jaeger et al., 2007] and radial pattern of tensile cracks forms finally. Such pattern has been also observed through X-Ray CT Scan on low strain rate experiments on sand [Desrués et al., 1996] and sandstone [Bésuelle et al., 2003]. This is not what is observed in pulverized samples of Carrara marble, where a new pattern of concentric fractures develops especially at high strain rates (Figure 1d). Several fractures propagate stress-shadowing

each other, a process theoretically predicted by statistical theory of high strain rate damage [Hild et al., 2003].

[18] The pulverized samples finally experience very large lateral expansion. For instance, the final diameter of sample M01 (Figure 1e) is about 3 cm (compared to the initial diameter of 2.5 cm), corresponding to a lateral expansion of 20%, which is enormous compared to the final uniaxial strain experienced by this sample ($\sim 3.4\%$; Table 1). It means that the sample, once pulverized, is not cohesive anymore and, therefore, centrifugal motion of grains is favored rather than creating new fractures across the grains. This inference is also supported by energy dissipation data (Figure 3c) as demonstrated below.

[19] In order to understand the energy related to damage mechanism, we estimate dissipated energy during loading by computing the quantity $\int_0^{\infty} \sigma \dot{\epsilon} dt$. This quantity corresponds to the area below the stress-strain curves of Figure 2. The way dissipated energy evolves with strain or strain rate depends on the microphysics of damage. Figure 3c shows the dissipated energy vs. strain. Below a strain of 1.3%, both the intact and split samples align along the same line, with a slope of 103 MJ/m^3 . It indicates that the damage mechanism is predominantly proportional to strain, suggesting an incremental damage. For pulverized samples, with strain above 1.3%, the data align with a slope of only 44 MJ/m^3 . This smaller slope means that it is easier to further accommodate strain once rocks get pulverized. In other words, in Figure 3c, with increasing strain, samples switched from a cohesive “rock-like” behavior (steep slope) to a granular “gouge-like” behavior (gentle slope) [Ben-Zion et al., 2011].

5. Application to Faults

[20] The above-discussed experimental results lead us to a few preliminary inferences about high strain rate damage in carbonates along seismic faults. In marble, to obtain the same degree of damage and fine grains as found in natural pulverized crystalline rocks [e.g., Dor et al., 2006], strain larger than 1.3% is needed for a strain rate of about 100 s^{-1} (Figure 3). At low strain rate, uniaxial quasi-static testing of sample M14 up to a total strain of 3% gave a split samples, with a large number of fractures, but not a diffuse microfracturing throughout the entire sample (Figure 1f). This result confirms that pulverization along faults is a high strain rate feature, perhaps a coseismic marker. Then, what are the conditions for pulverization of Carrara marble during an earthquake? Our experimental results show that a minimum strain of 1.3% at about 100 s^{-1} is necessary (Figure 3b). Let us assume subshear propagation along a mode II rupture at constant velocity. We assume a pure elastic case, not taking into account any viscoelastic behavior within the process zone at the fracture tip. We use the same formulas as Reches and Dewers [2005] and Doan and Gary [2009], with a critical stress intensity factor K_{II} equal to $30 \text{ MPa m}^{1/2}$, as in Reches and Dewers [2005], and typical Lamé coefficients $\mu = \lambda = 4 \text{ GPa}$, so that the Young modulus is 10 GPa as for our intact Carrara marble (Figure 2). We then obtain Figure 4, which shows that strain rate of 100 s^{-1} is attainable at distances from the fault core lower than 25 cm. The elastic properties of rock from the damage zone around a fault can be down to 50% lower than the protolith [Faulkner et al., 2006; Lewis and Ben-Zion, 2010], in which case high

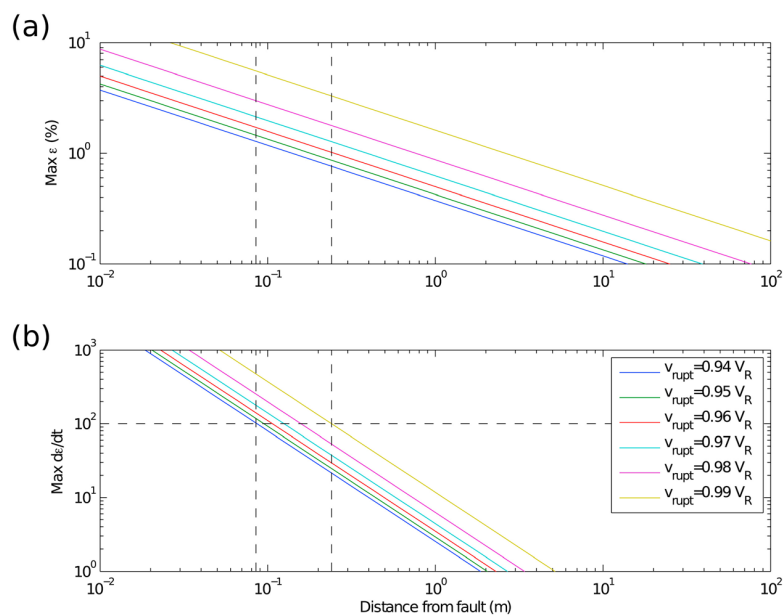


Figure 4. (a) Maximum strain and (b) strain rate experienced during an earthquake by a sample, depending on its distance to fault core. We assumed a subshear rupture of constant velocity v_{rupt} , proportional to the Rayleigh wave speed v_R . We used linear elastic fracture mechanics formalism, with critical stress intensity factor K_{II} equal to $30 \text{ MPa m}^{1/2}$, as by *Reches and Dewers* [2005], and typical Lamé coefficients $\mu = \nu = 4 \text{ GPa}$, corresponding to Young modulus of 10 GPa , as in Figure 2. Dashed lines in the distance vs. maximum strain rate diagram delimit the range of distances from the fault core where a strain rate of 100 s^{-1} is attained. At this distance, strain compatible with the limit strain of Figure 3 is attainable. Hence, pulverization of limestone is possible very close to the fault for a subshear rupture of constant velocity.

strain rate can be reached a little farther from the fault zone (for instance, for $\mu = \lambda = 1 \text{ GPa}$, a strain rate of 100 s^{-1} is attainable up to 40 cm away from the fault core; see auxiliary material).¹ This distance from the principal slip surface (40 cm) is usually well within the high shear strain zone (fault core) both in crystalline and in carbonate rocks [e.g., *Chester et al.*, 1993; *Frost et al.*, 2009]. Hence, it is probable that so close to the fault core, rock pulverization would be soon overprinted by the shear deformation leading to fault gouge development. This could be the case, in part, of the pulverized carbonate rocks signaled by *Agosta and Aydin* [2006] in central Italy. As pulverized rocks have been so far observed several tens of meters away from the fault core [*Dor et al.*, 2006, 2009], exceptional earthquakes, like supershear earthquakes [*Doan and Gary*, 2009] or a sudden acceleration of the rupture front must be invoked to reach pulverizing high strain rates so far from fault cores.

6. Conclusions

[21] In this paper, we presented how Carrara marble is damaged under uniaxial loading at high strain rate (c. 100 s^{-1}). At such strain rate, the transition from localized to diffuse damage is controlled by strain rather than strain rate and pulverization happens as soon as a strain above 1.3% is reached (Figure 3). This propensity for getting diffuse damage is paradoxical as pulverization is scarcely observed within carbonate rocks. To overstep this paradox, several explanations may be proposed. One is the fact that the Carrara

marble may not be so representative of sedimentary marine limestone, which is the main carbonate lithotype affected by faults in the crust [*Billi et al.*, 2003; *Agosta and Aydin*, 2006; *Woodcock and Mort*, 2008]. An alternative explanation may simply be that carbonate pulverization occurs very close to fault cores (Figure 4), where, subsequently, shear deformation masks all pulverization effects. In the case of bimaterial faults, the dissymmetry in elastic properties on each side of the fault leads to a weaker loading on the weaker side [*Ben-Zion and Andrews*, 1998]. More generally, damage can also affect the strength of the material. Experiments on granite, for instance, show that pulverizing rocks is easier as rocks accumulate damage through successive earthquakes (M.-L. Doan and V. d'Hour, Effect of initial damage on rock pulverization, submitted to *Journal of Structural Geology*, 2011). The efficiency of healing in carbonates at shallow depths [*Renard et al.*, 2000, *Hausegger et al.*, 2010] may explain the preserved carbonate outcrops observed within pulverized granite, as in the Lake Hughes area along the San Andreas Fault [*Dor et al.*, 2006]. Hence, carbonate rocks may be preserved when juxtaposed with granite. In any case, the discussed paradox calls for further investigation on high strain rate damage of carbonates.

[22] **Acknowledgments.** We warmly thank Gérard Gary for allowing us to work on the Split Hopkinson Pressure Bars of Ecole Polytechnique, and for providing much advice on experimental issues. We thank Mimmo (Petrolab) for thin-sections, The experiments were performed with the equipment of Pascal Charrier and Jacques Desrués (3SR laboratory) for X-Ray tomography of low strain-rate sample, and Jean-Benoit Toni (3SR laboratory) for the low strain rate experiment. We acknowledge funding from INSU 3F and UJF TUNES programs. We thank Yehuda Ben-Zion, Jacques Desrués and Gérard Gary for improving earlier versions of the manuscript. We

¹Auxiliary materials are available in the HTML. doi:10.1029/2011GL049169.

thank Erik Frost for his review that enabled us improve our text about the damage around carbonate faults.

[23] The Editor thanks Erik Frost for his assistance in evaluating this paper.

References

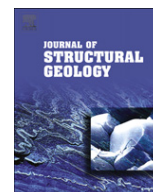
- Agosta, F., and A. Aydin (2006), Architecture and deformation mechanism of a basin-bounding normal fault in Mesozoic platform carbonates, central Italy, *J. Struct. Geol.*, *28*, 1445–1467, doi:10.1016/j.jsg.2006.04.006.
- Ben-Zion, Y., and D. J. Andrews (1998), Properties and implication of dynamic rupture along a material interface, *Geol. Soc. Am. Bull.*, *88*, 1084–1094.
- Ben-Zion, Y., K. A. Dahmen, and J. T. Uhl (2011), A unifying phase diagram for the dynamics of sheared solids and granular materials, *Pure Appl. Geophys.*, doi:10.1007/s00024-011-0273-7.
- Bésuelle, P., P. Baud, and T.-F. Wong (2003), Failure mode and spatial distribution of damage in Rothbach sandstone in the brittle-ductile transition, *Pure Appl. Geophys.*, *160*, 851–868, doi:10.1007/PL00012569.
- Billi, A. (2005), Grain size distribution and thickness of breccia and gouge zones from thin (<1 m) strike-slip fault cores in limestone, *J. Struct. Geol.*, *27*, 1823–1837, doi:10.1016/j.jsg.2005.05.013.
- Billi, A., and F. Storti (2004), Fractal distribution of particle size in carbonate cataclastic rocks from the core of a regional strike-slip fault zone, *Tectonophysics*, *384*, 115–128, doi:10.1016/j.tecto.2004.03.015.
- Billi, A., F. Salvini, and F. Storti (2003), The damage zone-fault core transition in carbonate rocks: Implications for fault growth, structure and permeability, *J. Struct. Geol.*, *25*, 1779–1794, doi:10.1016/S0191-8141(03)00037-3.
- Chen, W., and B. Song (2010), *Split Hopkinson (Kolsky) Bar: Design, Testing and Applications*, Springer, Berlin.
- Chester, F. M., J. Evans, and R. Biegel (1993), Internal structure and weakening mechanisms of the San Andreas Fault, *J. Geophys. Res.*, *98*, 771–786, doi:10.1029/92JB01866.
- Desrués, J., R. Chambon, M. Mokni, and F. Mazerolle (1996), Void ratio evolution inside shear bands in triaxial sand specimens studied by computed tomography, *Geotechnique*, *46*, 529–546, doi:10.1680/geot.1996.46.3.529.
- Doan, M. L., and G. Gary (2009), Rock pulverization at high strain rate near the San Andreas Fault, *Nat. Geosci.*, *2*, 709–712, doi:10.1038/ngeo640.
- Dor, O., Y. Ben-Zion, T. K. Rockwell, and J. Brune (2006), Pulverized rocks in the Mojave section of the San Andreas Fault Zone, *Earth Planet. Sci. Lett.*, *245*, 642–654, doi:10.1016/j.epsl.2006.03.034.
- Dor, O., C. Yildirim, T. K. Rockwell, Y. Ben-Zion, O. Emre, M. Sisk, and T. Y. Duman (2008), Geological and geomorphologic asymmetry across the rupture zones of the 1943 and 1944 earthquakes on the North Anatolian Fault: possible signals for preferred earthquake propagation direction, *Geophys. J. Int.*, *173*, 483–504.
- Dor, O., J. S. Chester, Y. Ben-Zion, J. Brune, and T. K. Rockwell (2009), Characterization of damage in sandstones along the Mojave section of the San Andreas Fault: Implications for the shallow extent of damage generation, *Pure Appl. Geophys.*, *166*, 1747–1773, doi:10.1007/s00024-009-0516-z.
- Evans, B., and D. L. Kohlstedt (1995), Rheology of rocks, in *Rock Physics and Phase Relation: A Handbook of Physical Constants*, AGU Ref. Shelf, vol. 3, edited by T. J. Ahrens, pp. 148–165, AGU, Washington, D. C.
- Faulkner, D. R., T. M. Mitchell, D. Healy, and M. J. Heap (2006), Slip on ‘weak’ faults by the rotation of regional stress in the fracture damage zone, *Nature*, *444*, 922–925, doi:10.1038/nature05353.
- Forrestal, M. J., T. W. Wright, and W. Chen (2004), The effect of radial inertia on brittle samples during the split Hopkinson pressure bar test, *Int. J. Impact Eng.*, *34*, 405–411.
- Fredrich, J. T., B. Evans, and T.-F. Wong (1989), Micromechanics of the brittle to plastic transition in Carrara marble, *J. Geophys. Res.*, *94*, 4129–4145, doi:10.1029/JB094iB04p04129.
- Frost, E., J. Dolan, C. Sammis, B. Hacker, J. Cole, and L. Ratschbacher (2009), Progressive strain localization in a major strike-slip fault exhumed from midseismogenic depths: Structural observations from the Salzach-Ennstal-Mariazell-Puchberg fault system, Austria, *J. Geophys. Res.*, *114*, B04406, doi:10.1029/2008JB005763.
- Gama, B. A., S. L. Lopatnikov, and J. W. Gillespie Jr. (2004), Hopkinson bar experimental technique: A critical review, *Appl. Mech. Rev.*, *57*, 223–250, doi:10.1115/1.1704626.
- Hausegger, S., W. Kurz, R. Rabitsch, E. Kiechl, and F.-J. Brosch (2010), Analysis of the internal structure of a carbonate damage zone: Implications for the mechanisms of fault breccia formation and fluid flow, *J. Struct. Geol.*, *32*, 1349–1362, doi:10.1016/j.jsg.2009.04.014.
- Hild, F., C. Denoual, P. Forquin, and X. Brajer (2003), On the probabilistic-deterministic transition involved in a fragmentation process of brittle material, *Comput. Struct.*, *81*, 1241–1253, doi:10.1016/S0045-7949(03)00039-7.
- Jaeger, J., N. G. W. Cook, and R. Zimmerman (2007), *Fundamentals of Rock Mechanics*, 4th ed., Blackwell, Oxford, U. K.
- Lenoir, N., M. Bornert, J. Desrués, P. Bésuelle, and G. Viggiani (2007), Volumetric digital image correlation applied to X-ray microtomography images from triaxial compression tests on argillaceous rock, *Strain*, *43*, 193–205, doi:10.1111/j.1475-1305.2007.00348.x.
- Lewis, M. A., and Y. Ben-Zion (2010), Diversity of fault zone damage and trapping structures in the Parkfield section of the San Andreas Fault from comprehensive analysis of near fault seismograms, *Geophys. J. Int.*, *183*, 1579–1595, doi:10.1111/j.1365-246X.2010.04816.x.
- Mitchell, T. M., Y. Ben-Zion, and T. Shimamoto (2011), Pulverized fault rocks and damage asymmetry along the Arima-Takatsuki Tectonic Line, Japan, *Earth Planet. Sci. Lett.*, *308*, 284–297, doi:10.1016/j.epsl.2011.04.023.
- Reches, Z., and T. A. Dewers (2005), Gouge formation by dynamic pulverization during earthquake rupture, *Earth Planet. Sci. Lett.*, *235*, 361–374, doi:10.1016/j.epsl.2005.04.009.
- Renard, F., J.-P. Gratier, and B. Jamtveit (2000), Kinetics of crack-sealing, intergranular pressure solution, and compaction around active faults, *J. Struct. Geol.*, *22*, 1395–1407, doi:10.1016/S0191-8141(00)00064-X.
- Rockwell, T., M. Sisk, G. Girty, O. Dor, N. Wechsler, and Y. Ben-Zion (2009), Chemical and physical characteristics of pulverized Tejon Look-out granite adjacent to the San Andreas and Garlock faults: Implications for earthquake physics, *Pure Appl. Geophys.*, *166*, 1725–1746, doi:10.1007/s00024-009-0514-1.
- Storti, F., A. Billi, and F. Salvini (2003), Particle size distributions in natural carbonate fault rocks: insights for non self-similar cataclasis, *Earth Planet. Sci. Lett.*, *206*, 173–186.
- Wechsler, N., E. E. Allen, T. K. Rockwell, G. Girty, J. S. Chester, and Y. Ben-Zion (2011), Characterization of pulverized granitoids in a shallow core along the San Andreas Fault, Little Rock, CA, *Geophys. J. Int.*, *186*, 401–417, doi:10.1111/j.1365-246X.2011.05059.x.
- Wilson, B., T. Dewers, Z. Reches, and J. Brune (2005), Particle size and energetics of gouge from earthquake rupture zones, *Nature*, *434*, 749–752, doi:10.1038/nature03433.
- Woodcock, N. H., and K. Mort (2008), Classification of fault breccias and related fault rocks, *Geol. Mag.*, *145*, 435–440.
- Yuan, F., V. Prakash, and T. Tullis (2011), Origin of pulverized rocks during earthquake fault rupture, *J. Geophys. Res.*, *116*, B06309, doi:10.1029/2010JB007721.

A. Billi, IGAG, Consiglio Nazionale delle Ricerche, c.o. Dipartimento Scienze della Terra, Sapienza Università di Roma, P.le A. Moro 5, 00185, Rome, Italy.

M.-L. Doan, Institut des Sciences de la Terre, Université Joseph Fourier, 1381 rue de la Piscine, F-38041 Grenoble CEDEX, France. (mai-linh.doan@obs.ujf-grenoble.fr)

Appendix C

Effect of initial damage on rock
pulverization along faults / Pure and
Applied Geophysics, 2012



Effect of initial damage on rock pulverization along faults

Mai-Linh Doan*, Virginie d'Hour

ISTerre, CNRS, Université Joseph Fourier, BP53, 38041 Grenoble Cedex 9, France

ARTICLE INFO

Article history:

Received 3 October 2011

Received in revised form

8 May 2012

Accepted 12 May 2012

Available online 23 May 2012

Keywords:

Dynamic damage

Pulverized rocks

Active fault

High strain rate experiments

Weibull theory

ABSTRACT

Pulverized rocks have been found in the damage zone around the San Andreas Fault, at distances greater than 100 m from the fault core. This damage is atypical in that it is pervasive and strain is not localized along main fractures as expected at these distances from the fault core. With high strain rate experiments, the authors have previously shown that above a strain rate threshold, the localization of strain along a few fractures is inhibited. Pulverized rocks may be generated by seismic waves at high frequency. Here we generalize these conclusions by discussing the effect of the initial fracture network in the sample on the transition from strain localization along a few fractures to diffuse damage throughout the sample. Experimental data are compared with statistical theory for fracture propagation. This analysis shows that the threshold in strain rate is a power law of initial fracture density and that a pre-damaged rock is easier to pulverize. This implies that pulverized rocks observed on the field may result from successive loadings.

© 2012 Elsevier Ltd. All rights reserved.

1. Introduction

Pulverized rocks have been observed near the San Andreas Fault (Wilson et al., 2005; Dor et al., 2006, 2009), and other large strike slip faults: Garlock Fault (Rockwell et al., 2009), Northern Anatolian Fault (Dor et al., 2008), and Arima-Takatsuki Fault (Mitchell et al., 2011). These rocks are found in outcrops of pervasively damaged rocks, which are sometimes as wide as several hundreds of meters. Due to the intense fracturing, individual samples typically crumble into powder when compressed by hand. Rockwell et al. (2009) have shown that the samples are microfractured, resulting in angular fragments about 100 μm in size. These rocks are only moderately chemically altered, so that their weakness cannot be attributed to weathering. High strain is one mechanism to explain the multiplicity of fractures: energy input rate is so high that it could not be accommodated by only a few fractures. A key observation is that the extensive damage of pulverized rocks is associated with small overall strain (Fig. 1). A second explanation for the diffuse damage pattern is high strain rate. With a higher energy supply rate, a single fracture with limited propagation speed cannot accommodate all of the applied energy. At higher strain rate, the finite velocity of stress waves also limits the expansion of the stress shadow zone around a major fracture, and interaction between fractures differs from the low strain rate case (Grady and Kipp, 1989; Hild et al., 2003b).

Pulverized rocks are localized within a few kilometers of the fault, with damage typically increasing closer to the fault core (Mitchell et al., 2011). This suggests that pulverization is related to fault activity. The origin of pulverized rocks is still debated, but most theories assume they are related to coseismic damage. The rarity of pulverization suggests that it is induced by an exceptional event, either by the tensile pulse predicted for rupture along bimaterial interfaces (Andrews and Ben-Zion, 1995), or by the Mach cone of a supershear rupture (Doan and Gary, 2009). Doan and Gary (2009) have shown experimentally that high strain rate loading can generate features similar to pulverization. They used samples from the Lake Hughes area of the Mojave segment of the San Andreas Fault (SAF), about 150 m away from the fault core. As a result of the proximity of the samples to the fault their experimental samples were pre-damaged.

The experiments reported here were conducted in a similar manner; a single, sudden and high energy loading event. Yet, thin sections of natural pulverized rocks reveal sealed microfractures (Fig. 1b), suggesting that the damage may be cumulative, and related to multiple loadings. These observations lead to the question: What is the effect of initial damage on the pulverization properties of rocks? In this paper, we investigate experimentally the effect of initial damage on the fragmentation process. We couple experimental results made on both pre-damaged and intact samples with the theory of Hild and Denoual (Hild et al., 2003a, 2003b; Denoual and Hild, 2000, 2002) to show that the threshold to pulverization decreases with greater initial damage. Hence, as

* Corresponding author. Tel.: +33 4 76 63 52 09; fax: +33 4 76 63 52 52.
E-mail address: Mai-Linh.Doan@obs.ujf-grenoble.fr (M.-L. Doan).

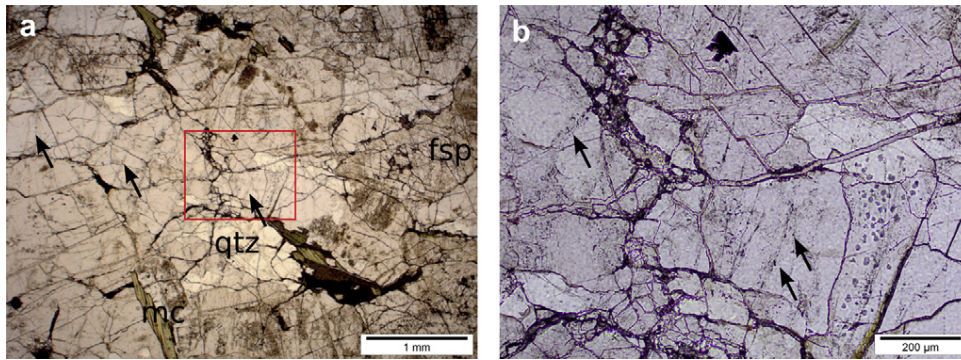


Fig. 1. (a) Thin section of a pulverized rock sampled near Mount Emma Road outcrop, located east of Palmdale, CA, along the Mojave segment of the San Andreas Fault (see also Fig. 3). Thin section was taken in plane polarized light. The outcrop location and description can be found in Fig. 1 of (Dor et al., 2006). Note the dense fracture network crosscutting grains and the preserved interlocked structure of the crystalline rock. The rock is severely damaged but with little shear displacement. Quartz (qtz) and feldspar (fsp) are affected, but the long, weak mica grain (mc) is only cleaved. (b) Zoom within the red rectangle of picture (a). Some sealed microfractures are highlighted by a series of fluid inclusions (black arrows), suggesting that the sample was previously damaged and healed (For interpretation of the references to color in this figure legend, the reader is referred to the web version of this article.).

rocks close to the fault get more and more damaged by successive loadings, pulverization becomes easier.

2. Experimental pulverization of rocks

2.1. Split Hopkinson pressure bars

When performing high strain rate testing, wave propagation time may not be negligible and the deformation measured at an individual strain gage may not be representative of the sample deformation (Nemat-Nasser, 2000). Moreover, classical servo-hydraulic machines have a limited loading velocity range leading to the use of Split Hopkinson Pressure Bars (SHPB) when applying strain rates above 100/s (Nemat-Nasser, 2000). In this study, we induce damage experimentally on protolith samples collected near the pulverized zone of the San Andreas Fault. The samples were loaded uniaxially at strain rate above 50/s, using the SHPB apparatus (Kolsky, 1963) at the Laboratoire de Mécanique des Solides of the École Polytechnique, Palaiseau, France.

Pulverized rocks have thus far only been documented in surface outcrops (Wilson et al., 2005; Dor et al., 2006, 2009, 2008; Mitchell et al., 2011) or in shallow boreholes at depths >50 m (Wechsler et al., 2011). The shallow borehole drilled along the San Andreas Fault provided samples free from surface alteration, that helped evaluate the relative timing of pulverization and surface alteration: Wechsler et al. (2011) argued that pulverization of outcrop rocks along the San Andreas Fault occurred recently, *i.e.* when the samples were at shallow depths. Therefore, we assume that unconfined conditions in our experiments are relevant for understanding rock pulverization, at least along the San Andreas Fault.

Each cylindrical sample is inserted between 2 bars and impacted by a striker bar arriving with a known speed (Fig. 2). The incident stress wave splits into reflected and transmitted waves when it reaches the sample. The incident and reflected waves are then measured with strain gauges on the input bar and output bar.

Classical processing of the SHPB assumes 1-D propagation of elastic waves, given the dimensions of the bars (3 m in length by 4 cm in diameter). Here, we have taken into account the dispersion and attenuation processes predicted by the 3D-model of Pochhammer and Chree (Graf, 1991). Due to our sampling rate of 1 MHz, we could reconstruct precisely forces and displacements at both ends of the specimen. We checked that the forces were identical at the input and output bars to verify that the sample was homogeneously loaded. Once the quasi-equilibrium of the specimen is

verified (equality of input and output forces), we calculated the history of stress, strain, and strain rate.

To ensure that the samples were loaded only once, the output bar is shorter than the input bar. Its exit extremity is free to move, allowing the output bar to move away from the sample before any reloading of the sample.

Experiments were conducted with strikers of various lengths (1.20 m, 0.9 m and 0.5 m), and with or without a lead foil inserted at the entry extremity of the input bar, which acts as a pulse shaper. By conducting experiments both with and without the pulse shaper we could decouple strain and strain rate.

2.2. Experiments done on samples from the damage zone of the San Andreas Fault

In this section, we briefly review the experiments (Doan and Gary, 2009) conducted on samples taken from near the San Andreas Fault, at the Lake Hughes outcrop. This outcrop has been described extensively in (Dor et al., 2006) (see their Figs. 1 and 5). Lying west of Palmdale city, CA, this outcrop is located in a narrow valley following the Mojave Segment of the San Andreas Fault. Although the fault itself is not visible, the damage zones of both sides of the fault are visible. The granite of the northern side is severely pulverized, with the intensity of pulverization decreasing rapidly (Fig. 3). The carbonate outcrop on the southern side is much less damaged. Samples were collected about 150 m from the fault core and were derived from the same protolith as the pulverized rocks but not pulverized themselves. The lithology of the samples is described in Table 1. We used this rock material to approximate the initial state before pulverization.

All samples have similar dimensions, 2.5 cm in diameter and 2.5 cm in length. The 1:1 aspect ratio offers a suitable compromise to minimize both stress shadow from sample ends (Paterson and Wong, 2005) and heterogeneity of stress in a long sample when the wave passes (Gama et al., 2004).

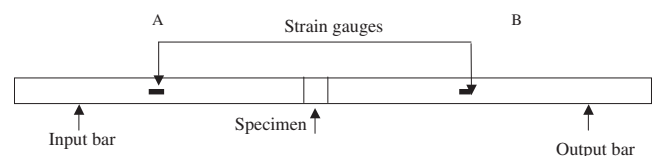


Fig. 2. Schematics of the split Hopkinson pressure bars.

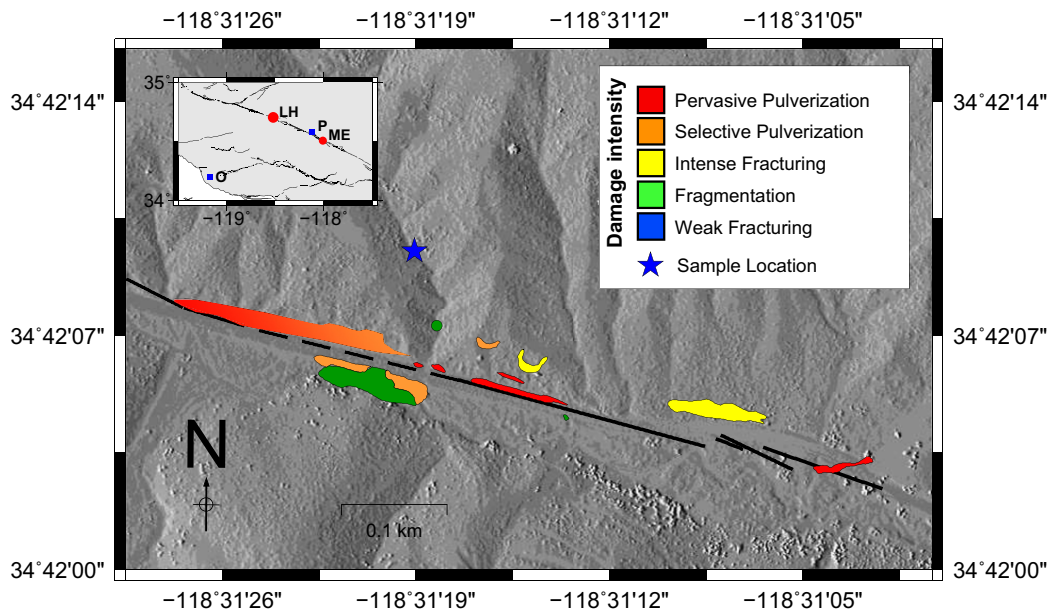


Fig. 3. Location of the samples used in the experiments. We overlay the pulverization map of Dor et al. (2006) and the location of the samples (blue star). We use the same color code as in Dor et al. (2006): red denotes pervasive pulverization, when all crystals in the sample can be crushed by hand; orange for selective pulverization, when some crystals remains intact; yellow for intense fracturing, when crystals retain the original grain size; green for distributed fracturing at the centimeter scale. Our sample can be classified as weakly fractured, with macroscopic large fractures visible in Fig. 5. The digital elevation data were obtained from the GEON project (Prentice et al., 2009). The map was made using Generic Mapping Tools (GMT) software (Wessel and Smith, 1998), using a basic cylindrical projection with a central meridian of longitude equal to $-118^{\circ}30'$ and a standard parallel of latitude equal to $34^{\circ}42'$. The inserted map shows location of some outcrops included in the text: Lake Hughes (LH) outcrop from which the samples for laboratory experiments were taken, Mont Emma Road (ME) outcrop, from which thin sections were made within pulverized rocks (Fig. 1). We also added the location of two major cities of the area, Palmdale (P) and Oxnard (O) (For interpretation of the references to colour in this figure legend, the reader is referred to the web version of this article.).

Three final states could be observed macroscopically:

1. the sample was not damaged
2. the sample was split axially in a few fragments, no more than 5. This is the typical damage observed when a rock sample is uniaxially loaded at low strain rate (Paterson and Wong, 2005).
3. the sample was shattered in multiple small fragments, smaller than the initial grain size of about 1.5 mm. This diffuse damage is reminiscent of pulverized rocks.

No intermediate state was observed between single fracturing and pulverization. Above a strain rate of 150/s, samples are pulverized

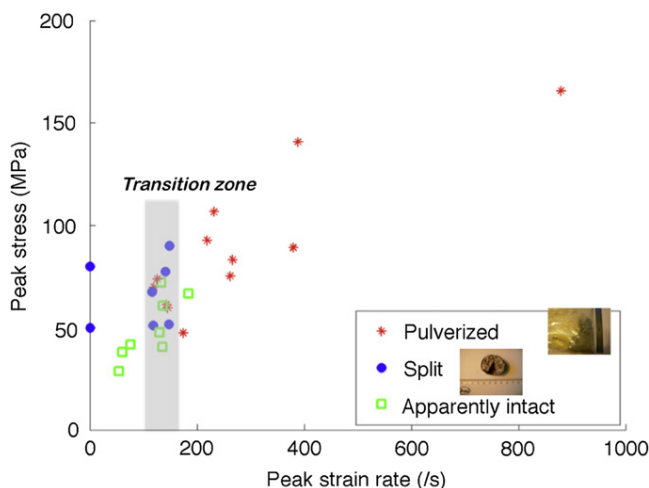


Fig. 4. Final states of damage after dynamic loading of granite from the San Andreas Fault. Results are gathered in a diagram showing strength versus maximum peak strain. There is a transition from single fracturing to multiple fragmentation at strain rates above 150/s (Doan and Gary, 2009).

and there is a sudden transition from failure along a small number of fractures to a pervasively pulverized damage. Doan and Gary (2009) infer that pulverized rocks in the field are the product of coseismic damage, with a strain rate larger than 150/s. They show that such a strain rate is not expected for usual earthquakes propagating at subshear rupture speed. They explain the origin of pulverized rocks as the damage generated by a shock wave, like the Mach wave accompanying a supershear rupture. A Mach wave is a solitary wave that decays slowly with distance. Bhat et al. (2007) show evidence of coseismic damage generated during a supershear rupture up to 5 km from the fault trace. A prediction of our experimental results is that the samples could be pre-damaged before testing, even though they were sampled 150 m from the fault core, a distance at which fracture density levels to the background level for most faults (Mitchell and Faulkner, 2009; Savage and Brodsky, 2011).

Several observations indeed suggest that, though not pulverized, the natural rock used in the first series of experiments was severely damaged. Fig. 5a shows a thin section of the initial state of one of the samples before loading. At the centimetric scale, microfractures are visible from inspection of the whole thin section. At higher magnification, microfractures are also visible at the millimetric and submillimetric scale. The sample is cohesive enough to withstand coring and moderate loading. Yet, experiments described in the next section give an uniaxial strength below 100 MPa, a low value for granitic rock (usually close to 200 MPa, as for Westerly granite (Heap and Faulkner, 2008)).

To investigate the effect of this initial damage on the high strain rate behavior of crystalline rocks, we conducted a further series of experiments of intact granitic rocks.

2.3. Experiments performed on intact rocks

To investigate the effect of damage, we used granite samples from Tarn, France. Fig. 6 shows a thin section of this rock and of the

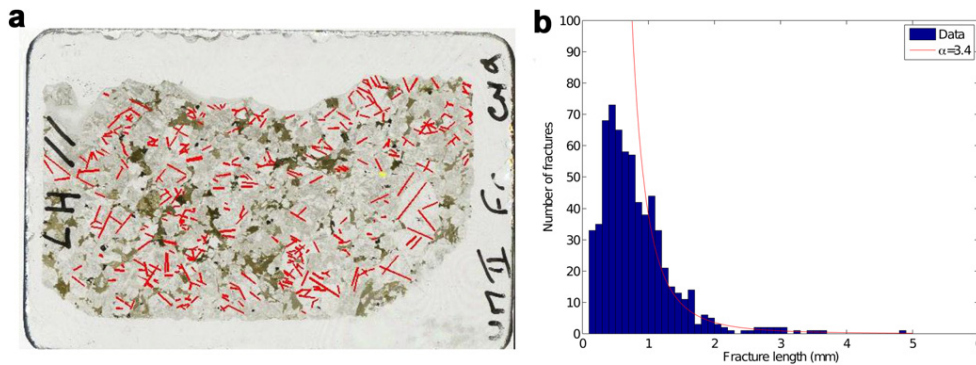


Fig. 5. (a) Thin section cut from a sample from the San Andreas Fault zone, before experiments. The thin section is 4.5 cm long and 2 cm wide. A total of 660 fractures are delineated. (b) Histogram of fracture lengths m delineated in figure (a). Most fractures are smaller than 2 mm. This length corresponds to a . The red line gives a power law fit, $p(l) \propto l^{-\alpha}$, of the fracture length distribution, with a power exponent $\alpha = 3.4$. The fit is poor for small lengths since statistics are not complete for small lengths.

San Andreas Fault rock for comparison. In both cases, the sample is granitic in composition, with a millimetric grain size, significantly smaller than the sample dimension (2.5 cm in diameter, about 2 cm in length). As with the granite near the San Andreas Fault, Tarn granite is slightly weathered, with mechanical alteration of the feldspar grains. Table 1 shows a similar modal composition for both rocks. Hence, we use the Tarn granite as a proxy for the intact, undamaged San Andreas Fault rocks.

Experiments on the Tarn granite are summarized in Fig. 7. It shows three distinct final macroscopic states (Fig. 8): intact, split in to a few fragments, or finely fragmented, equivalent to experiments on the SAF granite (Fig. 4). There is no intermediate state between the two latter stages, at least for the strain rates explored here.

Due to the loading duration being controlled by the striker length, there is always an ambiguity between strain rate and total strain accumulated (Doan and Billi, 2011). To compensate for this artifact, we used different strikers. We also used a pulse shaper to smooth the loading front (Chen and Song, 2010).

As shown in Figs. 7 and 9, pulverization can occur at both low and large strains. Very large strains are attained when the sample is pulverized and multiple fragments are ejected: the sample is no longer present to separate the input and output bars and we record artificially large strains.

There are fewer tests completed on the intact Tarn granite than on the pre-damaged San Andreas samples, yet a transition is still visible if we plot strength versus peak strain rate (Fig. 8). When loading at strain rates above 250/s, samples of Tarn granite fragment into fine grains. The transition threshold is larger than for the pre-damaged case. Rock strength also increases from 75 MPa to 150 MPa when the initial sample is less damaged.

One may speculate on the validity of the comparison between the experiments, as the high strain rate experiments were not conducted on the exact protolith of the damaged Lake Hughes granite. However, our results are consistent with two other studies, suggesting that our experiments are valid. The first is a series of experiments made on Westerly Granite by Yuan et al. (2011). This

paper has an outline very similar to Doan and Gary (2009), but is an independent study. They tested with Split Hopkinson Pressure Bars intact samples of Westerly Granite in unconfined and quasi-oedometric confined conditions. They find in unconfined conditions a transition to pulverization for strain rates above 250/s. The strength threshold was also about 150 MPa. The second is a theoretical model of pulverization developed by François Hild and co-authors (Hild et al., 2003b; Denoual and Hild, 2000), that is in agreement with our experimental results. This theory is presented in more detail within the next section, as we will use it to extrapolate our experimental results in the case of multiple loadings.

3. Statistical theory of pulverization

We studied experimentally the two extreme cases of (1) a pre-damaged sample and of (2) an intact sample. To generalize the conclusions drawn from our experimental data to any level of initial damage, we will refer to the theoretical model of transition from single fracturing to multiple fragmentation, that has been proposed by Hild, Denoual and co-workers (Denoual and Hild, 2000, 2002; Hild et al., 2003a, 2003b). This is a statistical theory that determines the strength of a brittle material, depending on whether it is fractured or pulverized. It is a variant of the Weibull statistical theory of strength. After reviewing the Weibull theory for the common low-strain-rate case, we will present the theory of the high strain rate case proposed by Denoual and Hild (2000). Once the two theories are described, a transition between them can be predicted. This section is mathematically-intensive. Symbols used in equations are summarized in Tables 2 and 3.

3.1. Description of the theory

3.1.1. Weibull hypotheses of rock failure

The Weibull model (Weibull, 1951) is a popular model to describe the failure of a sample by a single fracture. In a sample, there exist initial flaws, with different lengths, and hence different

Table 1

Modal composition of the rocks tested. Modal analysis was performed by random selection of 105 points of the available thin sections (two for the San Andreas Fault samples, one for the Tarn Granite). 95% confidence interval of the proportion of each mineral (in percent) is given between square brackets below the average composition.

| Sample | Quartz | K-Feldspar | Plagioclase | Biotite | Amphibole, sphene |
|-------------------|-------------|-------------|-------------|-------------|-------------------|
| San Andreas Fault | 28.7% | 33.3% | 20.3% | 16.0% | 1.6% |
| Thin section 1 | [24.5–33.3] | [28.8–38.1] | [16.5–24.5] | [12.6–19.9] | [0.6–3.5] |
| San Andreas Fault | 28.2% | 35.1% | 19.9% | 14.9% | 1.9% |
| Thin section 2 | [24.0–32.8] | [30.7–40.0] | [16.3–24.1] | [11.7–18.7] | [0.8–3.8] |
| Tarn Granite | 32.8% | 39.4% | 13.8% | 14.1% | 0% |
| | [28.4–37.4] | [34.8–44.1] | [10.6–17.4] | [10.9–17.7] | [0–0.9] |

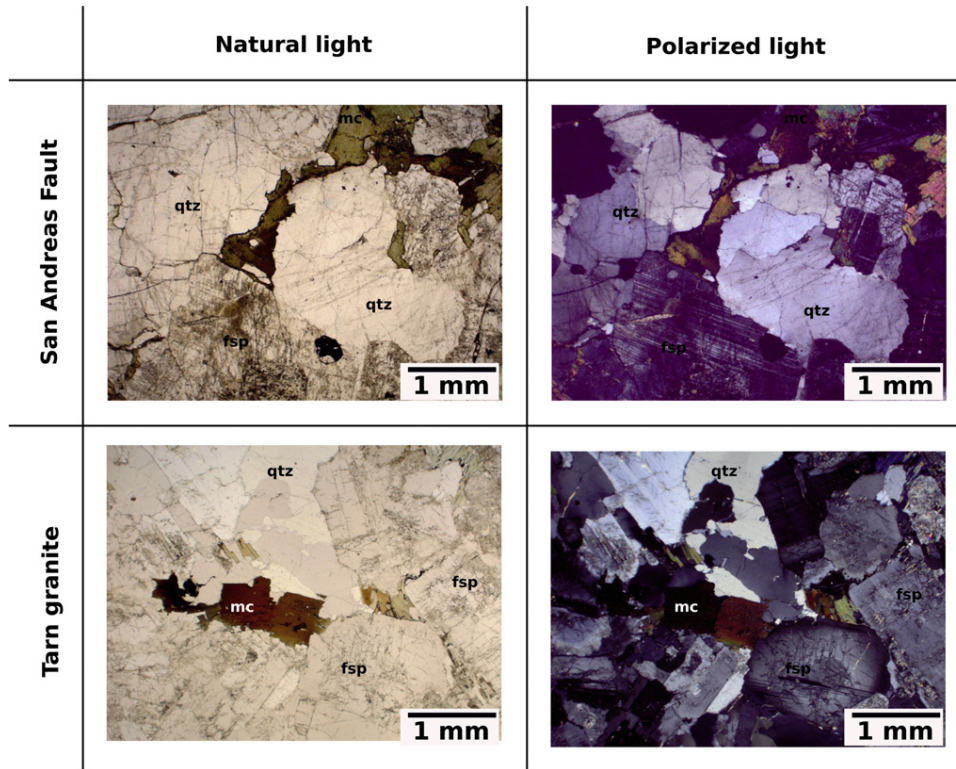


Fig. 6. Thin sections representative of the lithologies tested during the experiments described in this paper. Several minerals are visible: quartz (qtz), feldspar (fsp), mica (mc). Grain size is millimetric in both cases, and therefore much smaller than the sample size. Modal analysis made on the whole thin sections is given in Table 1.

strengths (Fig. 10a). The Weibull model assumes (1) that all flaws are loaded by the same stress, (2) that each flaw will have an independent probability to fail and (3) the breaking of a single fracture will induce the failure of the whole sample; this is the *weakest link hypothesis* (Fig. 10b).

Conditions (1) and (2) assume that the fracture density is low enough for fractures to develop independently, without stress-shadowing effects. If the load is heterogeneous, Hild et al. (2003b) introduced the concept of an effective volume $V_{\text{eff}} = Z_{\text{eff}}V$ to describe the homogeneously loaded portion of a sample in a rock.

Condition (3) can be understood with concepts from linear elastic fracture mechanics. Fractures act as stress concentrators. Linear elastic fracture mechanics states that at the tip of a fracture of length l , the stress σ is amplified as:

$$\sigma_{ij} = \frac{K}{\sqrt{2\pi r}} f_{ij}(\theta) \quad (1)$$

r is the distance to the fracture tip and θ the orientation to the fracture angle. f_{ij} is a known adimensional function. K is the stress intensity factor. Depending on the loading mode, the detail of its expression varies, but it retains the general form:

$$K = Y\sigma\sqrt{l}, \quad (2)$$

where Y is an adimensional geometrical factor and σ is the amplitude of the loading. For instance, for a mode I loading $K = \sigma\sqrt{\pi l}$.

Irwin (1957) have shown that if K exceeds a threshold value K_c then the fracture extends to reach a longer length l . According to Eq. (2), the stress intensity factor then increases. K_c could then be reached with a smaller stress σ : the strength of the fracture is smaller. This positive loopback explains why the failure of a major

flaw can develop catastrophically into the complete failure of the sample (Fig. 10b).

From a uniform stress field σ and a given fracture mode, Eq. (2) predicts that a fracture will fail if it exceeds a threshold length

$$L_c = \left(\frac{K_c}{Y\sigma} \right)^2 \quad (3)$$

We now explore the probability for the occurrence of a fracture longer than L_c .

3.1.2. Weibull statistical model of single fracturation

In most natural samples there is an initial network of fractures. The initial fracture density is labeled λ_0 . If we take a volume V , there is on average a number of N fractures within this volume, with $N = \lambda_0 V$. Fracture density is not the only fracture parameter controlling the sample strength. The length distribution of these fractures is also important. Each fracture has a probability of having a length between l and $l + dl$ given by the probability distribution function $p(l)$. The average density of fractures λ_{L_c} of length greater than a critical length is then $\lambda_{L_c} = \lambda_0 \int_{L_c}^{\infty} p(l) dl$. Hence, the probability of having k fractures of length greater than L_c within the volume V is then given by the Poisson statistics:

$$p_{V,L_c}(k) = \frac{(\lambda_{L_c} V)^k}{k!} e^{-\lambda_{L_c} V} \quad (4)$$

In the weakest link hypothesis, the probability of survival of the sample is given by $p_{V,L_c}(k = 0)$. If the sample does not survive, it fails, and hence the probability of failure is given by

$$p_F = 1 - p_{V,L_c}(0) = 1 - e^{-\lambda_{L_c} V} \quad (5)$$









| Sample | Peak strain rate (/s) | Peak stress (MPa) | Peak strain (%) | Final state | Photograph |
|--------|-----------------------|-------------------|-----------------|-------------|---|
| T1 | 708 | 313 | 4.12 | Pulverized | No picture |
| T2 | 51 | 97 | 0.25 | Intact | No picture |
| T7 | 755 | 201 | 8.26 | Pulverized |  |
| T9 | 518 | 159 | 4.74 | Pulverized |  |
| T10 | 150 | 126 | 0.13 | Split |  |
| T12 | 180 | 162 | 0.32 | Split |  |
| T13 | 289 | 160 | 0.66 | Pulverized |  |
| T14 | 258 | 144 | 0.74 | Split |  |
| T15 | 217 | 139 | 0.51 | Split |  |
| T17 | 251 | 153 | 0.56 | Pulverized |  |

Fig. 7. Summary of experiments performed on Tarn granite. For each sample, peak stress, peak strain, peak strain rate and a classification of the final damage are reported. When available, a photograph illustrating the post-mortem macrodamage of the sample is also included. The ruler in the photographs is graduated in centimeters.

This relationship scales with the volume under consideration (Weibull, 1951). For instance, if we are interested in a volume $\mathbb{V} = \nu \times V$, there is no failure in the volume \mathbb{V} if there is no failure within all the ν volumes of size V . All these events are independent and we obtain

$$p_{\mathbb{V},L_c}(0) = \left(p_{V,L_c}(0)\right)^\nu = e^{-\lambda_{L_c}\nu V} = e^{-\lambda_{L_c}\mathbb{V}} \quad (6)$$

Eq. (5) holds if we replace V by a larger volume \mathbb{V} . The expression of Weibull law is scale independent. Let us assume now that the size distribution $p(l)$ can be described by a power law $p(l) = Cl^{-\alpha}$, where C is a normalizing factor, dependent on the smallest fracture length. Then, we obtain a simple expression for λ_{L_c} :

$$\lambda_{L_c} = \lambda_0 \int_{L_c}^{\infty} Cl^{-\alpha} dl = -\lambda_0 C \frac{L_c^{1-\alpha}}{1-\alpha} \quad (7)$$

Using the above equation and Eq. (2), Eq. (5) then reduces to a Weibull distribution:

$$p_F = 1 - e^{-\left(\frac{\sigma}{\Delta\sigma}\right)^m} \quad (8)$$

where $m = 2(\alpha-1)$ and $\Delta\sigma = (K_c/Y)(m/2CV\lambda_0)^{1/m}$. m is called the shape parameter and $\Delta\sigma$ the scale parameter of the Weibull distribution. The maximum of the associated probability density function is reached at for $\sigma_{\max} = (m-(1/m))^{1/m}\Delta\sigma$ if $m > 1$. From Weibull equations, we obtain the average strength of a sample (Fig. 11):

$$\sigma_{F,\text{static}} = \int_0^{\infty} \frac{dp_F}{d\sigma} \sigma d\sigma = \frac{\Delta\sigma}{m} \Gamma\left[\frac{1}{m}\right] \quad (9)$$

where $\Gamma[x] = \int_0^{\infty} t^{x-1} e^{-t} dt$ is the gamma special function. Therefore the strength of the sample decreases with the initial density of

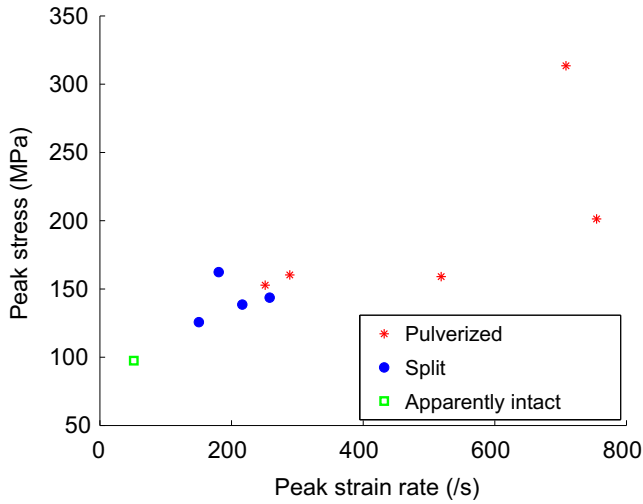


Fig. 8. Final states of damage after dynamic loading of Tarn granite. Results are gathered in a diagram showing strength versus maximum peak strain. As in Fig. 4, there is a transition from single fracturing to multiple fragmentation, but at a higher strain rate, above 250/s.

fractures λ_0 and with its volume, as we have more chance to find a fracture of critical length.

The Weibull model also recognizes that the heterogeneity of samples leads to a variability in sample strength. The standard deviation in sample strength is given as $\Delta\sigma_{F,static} = \Delta\sigma\sqrt{\Gamma(1 + (2/m)) - (\Gamma(1 + (1/m)))^2} \sim (\pi\Delta\sigma/\sqrt{6}m)$. This means that if m is very large, the Weibull distribution is very peaked, and hence has a more uniform strength distribution. By playing between the shape parameter m and the scale parameter $\Delta\sigma$, we can quantify the heterogeneity and the weakness of the sample. The Weibull model statistically predicts the strength of a sample based on microscopic fracture lengths (Jayatilaka and Trustrum, 1977).

To check the validity of the Weibull model for single-fracture samples, we estimated the m Weibull parameter for the pre-damaged San Andreas Fault samples using two approaches (Fig. 12). Fig. 5b gives the length distribution of fractures picked from a thin

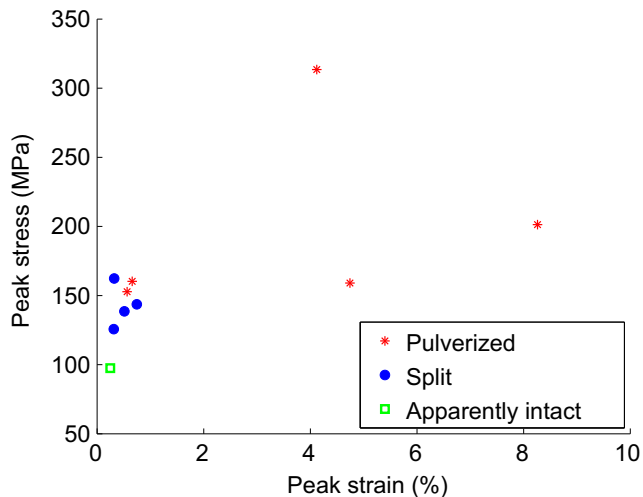


Fig. 9. Strain dependence on the transition from single fracturing to multiple fragmentation, from the summary of experiments in Fig. 5. The extremely damaged, pulverized rocks can withstand loading to artificially large strains; however, two cases (T13 and T17) also show that pulverization can occur at smaller strain.

Table 2
Table of symbols used within the equations of the text – Latin alphabet.

| Symbols | Meaning |
|----------------|---|
| c | Stress wave velocity |
| e | Euler number (~ 2.718) |
| K | Stress intensity factor |
| l | Length of fracture |
| L_c | Threshold length of fracture, for which $K > K_c$ or L_c . Fractures longer than L_c will propagate |
| m | Shape parameter of Weibull distribution. Representative of the sample homogeneity. |
| n | Number of dimensions of the problem (here 3) |
| p_F | Probability of failure |
| P_{ns} | Probability for a fracture longer than L_c to be not overshadowed by another fracture |
| $p_{V,L_c}(k)$ | Probability of having k fractures of length greater than L_c within the volume V |
| t_c | Characteristic time for a fracture to be interacting with surrounding fracture |
| t_f | Characteristic time for a fracture to reach failure under a constant stress rate $\dot{\sigma}$ |
| V | Volume of the sample |
| V_{eff} | Volume uniformly loaded by stress σ |
| Y | Geometrical factor intervening in stress intensity factor computation |
| Z_{eff} | Ratio between V_{eff} and V |

section, at a centimetric scale. The limited resolution of the image prevents the completeness of the fracture catalog for smaller fractures. Yet, the length distribution of the largest fractures can be roughly matched (Fig. 5) with a fractal coefficient $\alpha = 3.4$, giving an exponential value of $m = 2(\alpha - 1) = 4.8$. This result is slightly larger than the particle grain size distribution found with a laser granulometer by Wechsler et al. (2011), who obtained a grain size distribution matching a power law function with a coefficient α ranging from 2.5 to 3.1 for pulverized rocks collected in a borehole near Mount Emma outcrop along the San Andreas Fault (Fig. 3). We then determined the strength distribution for the samples that were split. The cumulative strength distribution is fitted with a Weibull distribution. We find a scale parameter $\Delta\sigma = 70$ MPa and a shape parameter $m = 5$, that is similar to the experimental value $m = 4.8$ found by fitting the microfracture length distribution. The Weibull theory gives satisfactory results for the samples that were pre-fractured.

Table 3
Table of symbols used within the equations of the text – Greek alphabet.

| Symbols | Meaning |
|---------------------------|---|
| α | Coefficient of the power law governing fracture length statistics |
| $\gamma(\nu, x)$ | Lower incomplete Gamma special function |
| $\Gamma(x)$ | Gamma special function |
| $\Delta\sigma$ | Scale parameter of Weibull distribution. Representative of the sample strength. |
| $\Delta\sigma_{F,static}$ | Standard deviation of the strength statistics of a sample quasi-statically loaded |
| λ_0 | Initial fracture density |
| λ_b | Density of fractures amenable to further propagation and that effectively break |
| $\lambda_{b,sat}$ | Maximum density of fractures that effectively break, at saturation |
| λ_s | Density of fractures amenable to further propagation but stress-shadowed by other fractures |
| λ_{L_c} | Density of fractures of length longer than L_c , i.e. of fracture amenable to propagation |
| σ | Applied stress |
| $\dot{\sigma}$ | Stress rate |
| $\dot{\sigma}_c$ | Transition stress rate from single fracture to multiple fragmentation |
| $\sigma_{F,dyn}$ | Average strength of a sample loaded at high strain rate |
| $\sigma_{F,static}$ | Average strength of a sample quasi-statically loaded |
| Ω_0 | Initial size of the shadow zone around a fracture |

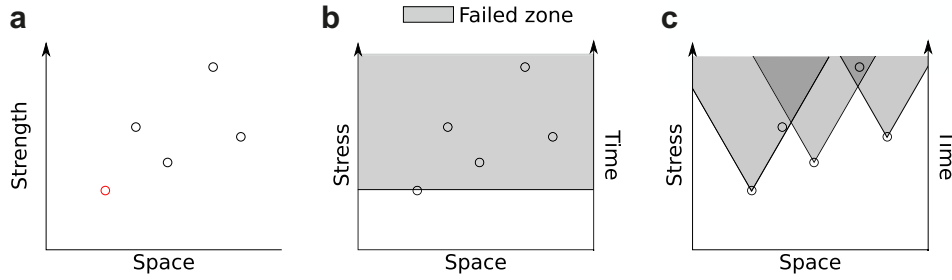


Fig. 10. Schematics of the different theories of failure. (a) Initial flaw model: There is an initial distribution of flaws scattered in space, with different locations, and different strengths. The sample is then loaded at a given stress rate (or strain rate in an elastic solid). There are two extreme cases: (b) Slow strain rate case: The sample is loaded so slowly that the propagation of the weakest flaw is considered instantaneous. Breaking the weakest flaw leads to the failure of the whole sample. (c) High strain rate case: The sample is loaded so rapidly that the finite fracture propagation speed cannot be ignored. This allows the propagation of multiple fractures at the same time. Yet not all fractures propagate, as some can be stress shadowed by other propagating flaws.

3.1.3. The Hild model of multiple fragmentation

When a sample is loaded rapidly, the physics of the interaction between flaws is altered (Fig. 10c). Stress wave propagation has to be taken into account. The weakest flaw takes a finite time to expand, during which time other cracks can also expand. But during that time, some fractures can also enter the shadow zone of others. Hence, the Weibull model has to be modified to take into account these two phenomena. This is what is achieved with the theory of Hild et al. (2003b), which we will summarize and reformulate in this section. Let us assume that a stress σ is applied homogeneously on the material. We saw in Section 3.1.2 that there

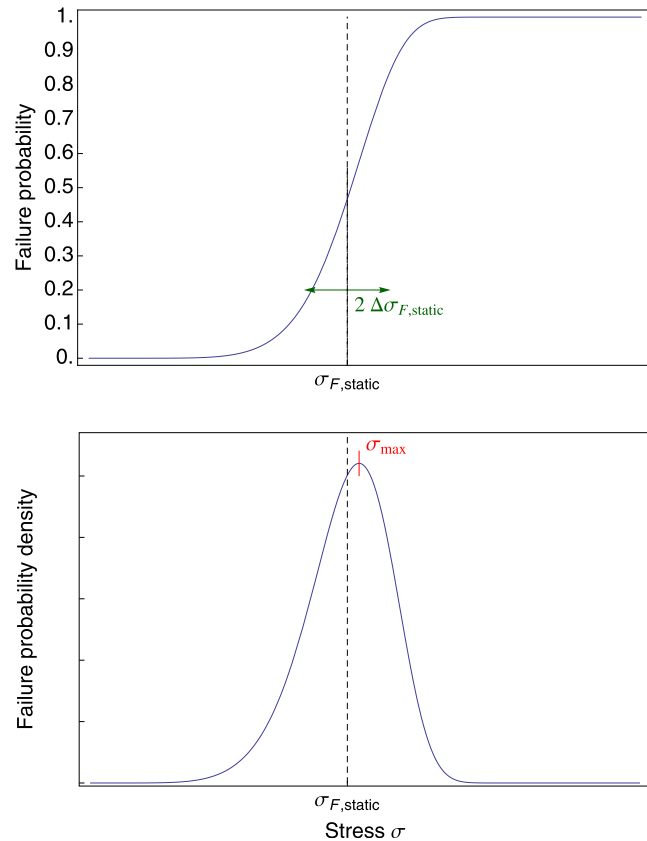


Fig. 11. Failure probability predicted by Weibull equation (Eq. (8)). The shape parameter m and the scale parameter $\Delta\sigma$ control the values of σ_{av} (Eq. (9)) and σ_{max} . In this graph, $m > 1$.

is an average density of fractures λ_{Lc} that may break for a stress smaller than σ . Combining Eqs. (3) and (7), λ_{Lc} expresses as

$$\lambda_{Lc} = \lambda_0 \frac{2C}{m} \left(\frac{Y\sigma}{K_C} \right)^m \quad (10)$$

However, only a fraction λ_b of them effectively break, as some are stress-shadowed. The density of shadowed fractures is denoted by λ_s .

$$\lambda_b = \lambda_{Lc} - \lambda_s \quad (11)$$

Let us assume that the area shadowed by an expanding flaw expands as $\Omega(t) = \Omega_0 \times (c(t-t_0))^n$, where n is the dimension of the problem (here $n = 3$), c is the fracture propagation speed, Ω_0 an adimensional coefficient controlling the size of the shadow zone and t_0 the start of fracture propagation. The sample is progressively loaded and stress increases with time: $\sigma = \dot{\sigma}t$. In the case of a purely brittle material, this is equivalent to loading at a constant strain rate. Let us suppose we are now at time t . At $t + dt$, we reach the stress $\sigma + (d\sigma/dt)dt$. At this higher stress, new cracks will begin to break, provided that their strength is between σ and $\sigma + (d\sigma/dt)dt$ and that they are not overshadowed:

$$\frac{d\lambda_b}{dt} = \frac{d\lambda_{Lc}}{dt} P_{ns} \quad (12)$$

We now address the question of how to compute P_{ns} , the probability not to be shadowed? A flaw is not overshadowed if there is no initial fracture on its horizon during previous time steps (Fig. 13). To estimate this, let us consider the probability that a fracture can be overshadowed by another fracture that would have initiated at time t_0 and $t_0 + dt_0$. This is equivalent to slicing the horizon (dashed lines of Fig. 13) several times between t_0 and $t_0 + dt_0$ (horizontal lines of Fig. 13). This is given by the Poisson process that involves the probability of finding a fracture of strength $(d\lambda_{Lc}/d\sigma)(d\sigma/dt)dt = d\lambda_{Lc}/dt|_{t_0} dt_0$ in the affected volume $\Omega(t-t_0)$. The probability that no fracture appears is

$$dP_{ns} = \exp\left(-\frac{d\lambda_{Lc}}{dt}\bigg|_{t_0} \Omega(t-t_0)dt_0\right) \quad (13)$$

We then integrate Eq. (13) for all previous time steps, until $t_0 = 0$, using the scaling relationship of the Weibull distribution (Eq. (6)). The probability for a fracture not being shadowed is then:

$$P_{ns} = \exp\left(-\int_0^t \frac{d\lambda_{Lc}}{dt}\bigg|_{t_0} \Omega(t-t_0)dt_0\right) \quad (14)$$

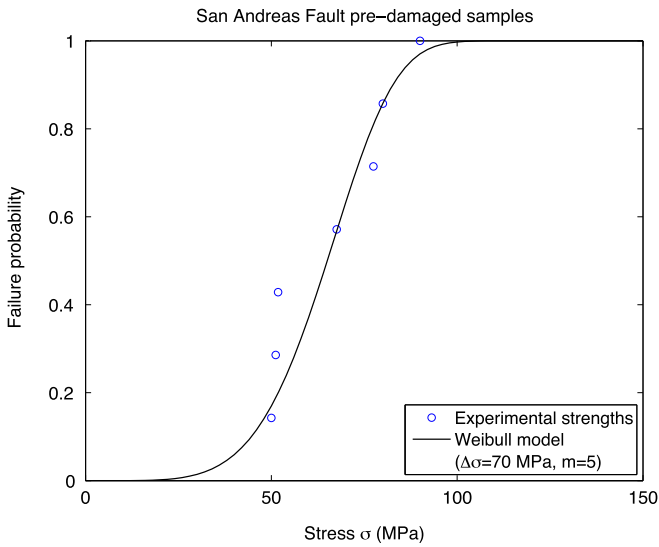


Fig. 12. Experimental determination of the Weibull parameters for the pre-damaged samples from the San Andreas Fault. We consider only the strength of the samples that were single-fractured. The cumulative probability density function is then fitted with a cumulative Weibull distribution, as in Fig. 11. Experimental Weibull parameters are $\Delta\sigma = 70$ MPa and $m = 5$.

We then integrate this equation using the expression of λ_{L_c} from Eq. (10) to obtain

$$P_{ns} = \exp \left[-\lambda_0 \frac{2C}{m} \Omega_0 c^n \frac{m!n!}{(m+n)!} t^{m+n} \left(\frac{\dot{\sigma} Y}{K_C} \right)^m \right] \quad (15)$$

Note that we can simplify the above expression as $P_{ns} = e^{-(m!n!/(m+n)!)\lambda_{L_c}(t)\Omega_0(ct)^n}$, but we prefer to write $P_{ns} = e^{-(t/t_c)^{m+n}}$ to highlight the characteristic time for fracture interaction through stress waves:

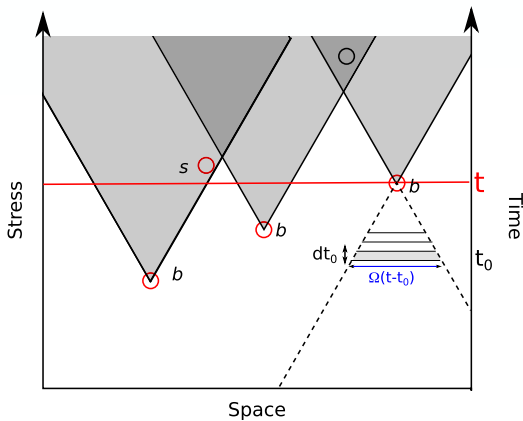


Fig. 13. Graphical representation of the concepts developed in the case of multiple fractures. For a given stress, there are a few preexisting flaws that have a lower stress than σ (red circle, labeled with a subscript c in the main text). Some of them are effectively initiated (subscript b) and their shadow zones (shaded areas) expand as they propagate. Others flaws cannot be activated (subscript s) because they fall within the shadow zone of an initiated crack. To investigate the probability of falling within a shadow zone, we delineate the horizon of the fracture (dashed lines) projected backwards in time, or equivalently backwards in stress as $\sigma = \dot{\sigma} dt$. The probability that a crack breaks is computed by combining the probability for an existing flaw to be within the influence area between t_0 and $t_0 + dt$ (For interpretation of the references to color in this figure legend, the reader is referred to the web version of this article).

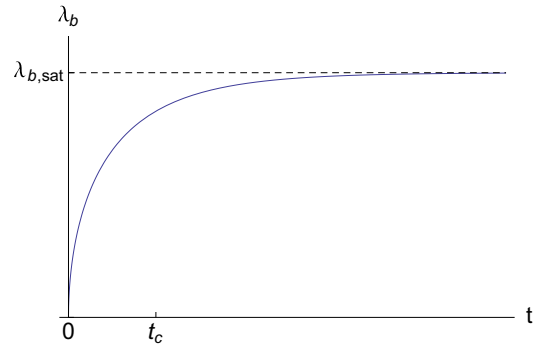


Fig. 14. Time evolution of breaking fracture with time, as predicted by Eq. (18). The fracture population increases with a power law of time, but saturates due to stress-shadowing between propagating fractures.

$$t_c = \left[\frac{2C\lambda_0\Omega_0 m!n!c^n \left(\frac{\dot{\sigma} Y}{K_C} \right)^m}{m(m+n)!} \right]^{-\frac{1}{m+n}} \quad (16)$$

The equation is rather large, yet it expresses some intuitive ideas: the characteristic time for fracture interaction decreases with the initial density of fractures λ_0 , with the loading rate $\dot{\sigma}$, the minimal size of the shadow zone around each Ω_0 and with the stress wave velocity c . The characteristic time t_c is to be compared with another characteristic time: the time t_f for the loading to lead to new fracture t_f . We can re-express Eq. (10) as $\lambda_{L_c} = \lambda_0(t/t_f)^m$ with

$$t_f = \frac{K_C}{\dot{\sigma} Y} \left(\frac{m}{2C} \right)^{\frac{1}{m}} \quad (17)$$

From Eqs. (10), (12) and (15), we derive λ_b , the density of fractures that will effectively break at stress σ :

$$\lambda_b = \lambda_0 \frac{m}{m+n} \left(\frac{t_c}{t_f} \right)^m \gamma \left[\frac{m}{m+n}, \left(\frac{t}{t_c} \right)^{m+n} \right] \quad (18)$$

where $\gamma[v, x] = \int_0^x t^{v-1} e^{-t} dt$ is the lower incomplete gamma function. The time evolution predicted by the above equation is given by Fig. 14. As $\gamma[v, t] \sim (t^v/v)$ at short times, $\lambda_b \sim \lambda_0(t/t_f)^m$: the more homogeneous the distribution of flaw strengths, the higher is m , and the more sudden is the simultaneous growth of fractures. Note that at small times, $\lambda_b(t) \sim \lambda_{L_c}(t)$: the stress-shadowing phenomenon is not yet efficient. The breaking fractures density saturates rapidly to $\lambda_{b,sat} = \lambda_0(m/m+n)\Gamma[m/m+n](t_c/t_f)^m$, where $\Gamma[x]$ is the Euler gamma function ($\Gamma[v] = \gamma[v, \infty]$). We see that the density of fractures that will effectively break increases if the shadowing process is slow (large t_c) compared to the fracture initiation duration t_f . The above equation can be expressed in terms of applied stress rather than time, by introducing a critical stress $\sigma_c = \dot{\sigma} t_c$. The critical stress scales as $\dot{\sigma}^{n/(m+n)}$.

Computing analytically the strength of the sample is difficult. We can no longer use the Poisson process underlying the Weibull Eq. (5) as the failures of all subparts of the samples are not independent events anymore, because of the stress-shadowing process. Instead, Denoual and Hild (2000) use a mean-field theory by introducing the concept of macroscopic damage D to exploit the density of broken fractures. They take as a proxy of damage the probability $D = 1 - P_{ns}$. This damage parameter is then inserted in a mean-field theory of stress screening, similar to the strategy developed by Grady and Kipp (1989): the stress that has been considered so far is an effective stress that is different from the applied stress $\sigma_{app} = (1-D)\sigma$. The dynamic strength $\sigma_{F,dyn}$ of the

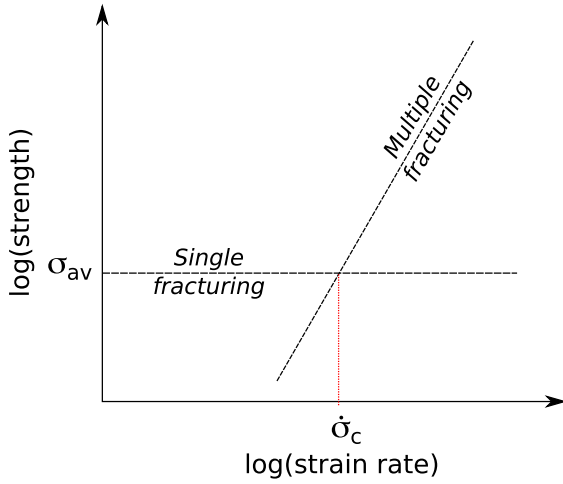


Fig. 15. Strength depends on the pulverization regime. In the case of a single fracture, strength is independent of strain rate. In case of pulverization, strength is a power law of strain rate. The transition between the two regimes happens for a characteristic stress $\dot{\sigma}_c$.

sample is the maximum of the stress applied during the loading. This happens when $(d\sigma/dt) = (d/dt)((\dot{\sigma}t)P_{ns}) = 0$, i.e. for $t_{\max} = (1/m+n)^{(1/m+n)}t_c$. The maximum applied stress is therefore $\sigma_{F,\text{dyn}} = e^{-1/m+n}\sigma_c$, whose full expression is

$$\sigma_{F,\text{dyn}} = \left[\frac{2eC\lambda_0\Omega_0 m! n! c^n \left(\frac{Y}{K_C}\right)^m}{m(m+n)!} \right]^{\frac{1}{m+n}} \dot{\sigma}_c^{\frac{n}{m+n}} \quad (19)$$

Dynamic strength increases with strain rate, with a power law of exponent $(n/m+n)$. Higher strain rate indeed results in smaller fragments, as shown by the experiments of Section 2 but also by Grady and Kipp (1989). This increases the fracture energy created during damage of the rock. This contrasts with the quasi-static loading case, for which strength is independent of strain rate.

3.2. Prediction on the effect of damage on the transition

These theoretical results show that rock strength varies with stress rate (hence for a pure brittle solid, with strain rate). The variation is schematically described in Fig. 15. For a single fragmentation problem, strength is constant. For a multiple fragmentation problem, strength increases as a power law of stress rate. The transition between the two regimes happens when $\sigma_{F,\text{static}} = \sigma_{F,\text{dyn}}$. If we use the damage theory of Denoual and Hild (2000), we get a transition strain rate of

$$\dot{\sigma}_c = \left(\frac{2C\lambda_0}{m}\right)^{-\frac{1}{m}} \frac{K_C c}{Y} \left[\frac{e\Omega_0 n! m!}{(m+n)!} \right]^{\frac{1}{n}} \left(\frac{\Gamma\left[\frac{1}{m}\right]}{m} \right)^{\frac{m+n}{n}} V^{-\frac{m+n}{mn}} \quad (20)$$

This can be also more compactly written as

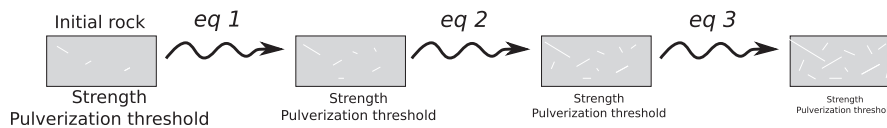


Fig. 16. Schematic evolution of damage as successive earthquakes (eq) further damage the rock. Both rock strength and the strain rate pulverization threshold decrease with successive earthquakes. This leads to a feedback process whereby diffuse damage is increasingly facilitated during subsequent loadings. In other words, the rock becomes progressively pulverized.

$$\dot{\sigma}_c = \left[\frac{e\Omega_0 n! m!}{(m+n)!} \right]^{\frac{1}{n}} \left(\frac{\Gamma\left[\frac{1}{m}\right]}{m} \right)^{\frac{m+n}{n}} \Delta\sigma c V^{-\frac{1}{n}} \quad (21)$$

The threshold in stress rate depends on $\Delta\sigma$, the scale parameter of the Weibull distribution used in the static case, divided by the characteristic time for elastic wave to travel the sample $V^{(-1/n)}/c$ and by an adimensional factor that depends on the shape parameter m of the Weibull distribution, i.e. the initial fracture size distribution of the sample. This highlights several features. The transition threshold $\dot{\sigma}_c$ from single fracturing to fragmentation decreases with the initial density of fractures λ_0 , with an exponent $1/m$. It also decreases with the volume V of the rock loaded, with an exponent $(m+n/mn)$. The homogeneity of the sample, described by the Weibull shape parameter m , also affects the transition threshold. The three parameters also affect the static strength of the sample (Eq. (9)).

The size dependence might have been problematic to the applicability of our experiments to a fault zone. Yet, pulverized rocks are recognized in the field as (1) a rock sample that is easily crushed within a person's hand and (2) as a rock whose initial structure is preserved, i.e. a rock that has experienced little strain. Condition (1) is tested with samples a few centimeters long, which is the size of our experimental samples. Hence, we consider that the strength and transition from single fracturing to fragmentation determined from our experiments are valid.

The theory predicts a diminution of the strength and the transition threshold to pulverization with initial damage, as they both scale as $\lambda_0^{(-1/m)}$. This confirms the experimental results of Section 2. The intact rock has a static strength of about 150 MPa and a transition strain rate of about 250 s^{-1} . The pre-damaged rock has a strength of 75 MPa, only half the strength of the intact rock. The transition strength for the pre-damaged rock also decreases by almost a factor of two, falling to about 150 s^{-1} . Hence, the theory provides a correct prediction of our experimental results.

4. Application to active faults: development of a zone of pulverized rocks after multiple earthquakes

The diminution of the strength and of the pulverization threshold suggests a scenario for pulverization along active faults in which rocks are pulverized by successive earthquakes (Fig. 16). A first earthquake loads at high frequency the surrounding rocks. If a rupture generates enough high frequencies, the damage is diffuse: multiple fractures propagate, and any decimetric fragment near the fault zone becomes diffusively damaged. The damage induces a reduction in strength of the rock near the fault. It also lowers the threshold in strain rate to switch from localized damage to diffuse damage (i.e. pulverization). It would be easier for the next earthquake to also damage diffusively all the rocks around the fault zone. With successive loadings, the rocks around the fault zone get progressively finely pulverized.

Pulverized rocks have only been identified recently (Wilson et al., 2005). Why don't we see more pulverized rocks? If loading happens at too low a strain rate, damage is localized along a few

fractures. In the portions which experienced little fracturing, their strength and strain rate threshold to pulverization are not modified. Hence, further loading would localize on the weak fractured area but not on the background rock left intact. The diffuse damage pattern found in outcrops of pulverized rocks would not be found if no sufficiently high strain rate loading occurred. Doan and Gary (2009) have demonstrated that such high strain rate loading is rare but may occur, for instance, associated with supershear earthquakes.

The feedback process described above may explain the commonly observed decrease in damage with distance from the fault, including in the case of pulverized rocks. Faulkner et al. (2010) review published profiles of decay of microfracturing with distance from the fault core. If we compare Fig. 4 of Faulkner et al. (2010) with the microfracture decay profile for the pulverized granite of the Arima-Takatsuki fault (Mitchell et al., 2011), we observe that the decay rate for the pulverized fault is among the highest, and as rapid as for the outcrop described by Vermilye and Scholz (1998). Pulverization is very intense close to the Arima-Takatsuki fault, but decays rapidly with distance, although the absolute microfracture density is above what is typically observed along non-pulverized faults. This is also shown on the pulverization map of the Lake Hughes outcrop (Dor et al., 2006), reported in Fig. 3, where pulverized outcrop is localized in patches. This may be explained by our results. Before pulverization, rocks closer to the fault core are more damaged and hence easier to pulverize. During the first pulverizing events, they get even more damaged than rocks located farther from the fault. With successive events, they would experience intense comminution compared to rocks further away. Pulverized rocks would then be found highly localized close to the fault.

The distribution of pre-damaged rocks may also explain the paradox of the Lake Hughes outcrop along the Mojave segment of the San Andreas Fault (Dor et al., 2006), where pulverized granite and undamaged limestone are found on the same side of the fault. The two rocks are likely to have different strengths and are therefore likely to pulverize in different ways. If earthquakes started to homogeneously damage the granite but not the limestone, the feedback loop described above would further differentiate the two rock behaviors relative to loading. Granite would become progressively damaged and easier to pulverize, while the carbonate rock would stay relatively intact and harder to damage.

Several pulverized outcrops have an asymmetric damage pattern (Dor et al., 2006; Mitchell et al., 2011) that has been attributed to the high frequency tensile pulse on the strongest side generated by an earthquake along a bimaterial fault (Shi and Ben-Zion, 2006). As the strongest side gets more damaged and becomes less strong, mature bimaterial faults may not be able to generate such high frequency pulses. Several arguments are in favor of the persistence of the high frequency pulse: (1) The development of an asymmetric pulse is controlled by mechanical properties at the kilometeric scale (2) Pulverized rocks have so far been found only at the surface or at shallow depths (Wechsler et al., 2011). We add a third argument: weaker rocks are more easily pulverized, and if the strongest side experienced pulverization previously, it would become more amenable to further pulverization. This could explain the sharp asymmetry in distribution of pulverized rocks along bimaterial faults.

In this feedback process leading to pulverization, we have ignored the healing process that follows earthquake events. Healing would seal fractures by a wide range of processes that depend on the size of the fractures (Gratier and Gueydan, 2007): thin fractures experience self-healing within days, a process driven by minimization of surface energy, whereas larger fractures require years to heal by pressure solution. Hence large scale-healing of

faults is expected to be driven by pressure solution (Gratier, 2011). Pressure-solution efficiency depends on the solubility of the mineral involved. Dissolution of feldspar and quartz are more efficient at high temperatures, below 5 km depth, whereas dissolution of calcite is more efficient at low temperatures, above 3 km depth for a classical geothermal gradient of 30 K/km (Gratier et al., 2003). For instance, samples taken within the San Andreas Fault at the SAFOD borehole show evidence of intense sealing by calcite, some evidence of feldspar dissolution, but quartz is intact (Gratier et al., 2011). In the case of the pulverized rocks found along the San Andreas Fault, self-healing of former thin fractures is evidenced by the presence of lineaments of inclusion planes. But Fig. 1 shows no sign of dissolution of Feldspar or quartz, consistent with the fact that these rocks were pulverized in the near surface environment. As these rocks are crystalline, no calcite cementation is found. Hence pressure solution did not happen within these rocks: only the thin intragranular fractures with no mismatch would heal. This may explain why the pulverized rocks found along the Mojave segment of the San Andreas Fault (Dor et al., 2006) are still damaged whereas the last large recorded event in the area occurred about 150 years earlier (1857 Fort Tejon earthquake).

5. Conclusions

In this paper we have presented several pieces of evidence suggesting that rocks are easier to pulverize when they are pre-damaged. We first presented experimental results from high strain-rate loading experiments on both pre-damaged and intact granite. Pre-damaged granite is pulverized if the strain rate is higher than 150/s. Instead, two independent studies find a strain rate threshold of 250/s for intact granite. The strain rate threshold is roughly proportional to the sample strength at low strain rate. These experimental results are consistent with the statistical theory of high strain rate proposed by Denoual and Hild (2000) and Hild et al. (2003b).

We propose a scenario in which pulverized rocks may result from successive earthquakes, instead of pulverization occurring by a single event. Yet, to initiate the feedback process leading to pulverization, diffuse damage of rocks around the fault is required to occur by high strain rate loading. This suggests that pulverized rocks are markers of extreme loading. This is consistent with the persistent features associated with the process that may generate high frequency waves around a fault: bimaterial faults (Andrews and Ben-Zion, 1995), or the low roughness of segments prone to supershear rupture (Bouchon et al., 2010).

Acknowledgments

We warmly thank Gérard Gary for accepting us working on the Split Hopkinson Pressure Bars of École Polytechnique, and for providing many advices on experimental issues. We thank Christophe Nevado and Fayçal Soufi for their thin sections. We acknowledge funding from INSU 3F and UJF TUNES programs. We thank Yehuda Ben-Zion, Andy Rathburn and Gérard Gary for their comments on earlier versions of the manuscript. We are grateful to Tom Mitchell and an anonymous reviewer for their constructive reviews and to Mark Simons and Steve Smith for mending the English of the final version of the manuscript

References

- Andrews, D.J., Ben-Zion, Y., 1997. Wrinkle-like slip pulse on a fault between different materials. *J. Geophys. Res.* 102, 553–571.
- Bhat, H.S., Dmowska, R., King, G.C.P., Klinger, Y., Rice, J.R., 2007. Off-fault damage patterns due to supershear ruptures with application to the 2001 M_w 8.1

- Kokoxili (Kunlun) Tibet earthquake. *J. Geophys. Res.* 112, 1–19. doi:10.1029/2006JB004425.
- Bouchon, M., Karabulut, H., Bouin, M.-P., Schmittbuhl, J., Vallée, M., Archuleta, R., Das, S., Renard, F., Marsan, D., 2010. Faulting characteristics of supershear earthquakes. *Tectonophysics* 493 (3–4), 244–253.
- Chen, W.W., Song, B., 2010. Split Hopkinson (Kolsky) Bar Design, Testing and Applications. Mechanical Engineering Series. Springer, New York.
- Denoual, C., Hild, F., 2000. A damage model for the dynamic fragmentation of brittle solids. *Comp. Meth. Appl. Mech. Eng.* 183 (3–4), 247–258.
- Denoual, C., Hild, F., 2002. Dynamic fragmentation of brittle solids: a multi-scale model. *Eur. J. Mech. A* 21 (1), 105–120.
- Doan, M.-L., Gary, G., 2009. Rock pulverisation at high strain rate near the San Andreas Fault. *Nat. Geosci.* 2, 709–712.
- Doan, M., Billi, A., 2011. High strain rate damage of Carrara marble. *Geophys. Res. Lett.* 38 (38), L19302. doi:10.1029/2011GL049169.
- Dor, O., Ben-Zion, Y., Rockwell, T.K., Brune, J., May 2006. Pulverized rocks in the Mojave section of the San Andreas fault zone. *Earth Planet. Sci. Lett.* 245, 642–654.
- Dor, O., Yildirim, C., Rockwell, T.K., Ben-Zion, Y., Emre, O., Sisk, M., Duman, T.Y., 2008. Geological and geomorphologic asymmetry across the rupture zones of the 1943 and 1944 earthquakes on the North Anatolian Fault: possible signals for preferred earthquake propagation direction. *Geophys. J. Int.* 173 (2), 483–504.
- Dor, O., Chester, J.S., Ben-Zion, Y., Brune, J.N., Rockwell, T.K., 2009. Damage characterization in sandstones along the Mojave section of the San Andreas fault with a new method: implications for the depth and mechanism of rock pulverization. *Pure Appl. Geophys.* 166 (10–11), 1747–1773.
- Faulkner, D.R., Jackson, C.A.L., Lunn, R.J., Schlische, R.W., Shipton, Z.K., Wibberley, C.A.J., Withjack, M.O., 2010. A review of recent developments concerning the structure, mechanics and fluid flow properties of fault zones. *J. Struct. Geol.* 32 (11), 1557–1575. doi:10.1016/j.jsg.2010.06.009.
- Gama, B.A., Lopatnikov, S.L., Gillespie Jr., J.W., 2004. Hopkinson bar experimental technique: a critical review. *Appl. Mech. Rev.* 57 (4), 223–250.
- Grady, D., Kipp, M., 1989. Dynamic rock fragmentation. In: Atkinson, B. (Ed.), *Fracture Mechanics of Rocks*. Academic Press, pp. 429–475.
- Graf, K.F., 1991. *Wave Motion in Elastic Solids*. Dover Publications.
- Gratier, J.-P., Favreau, P., Renard, F., 2003. Modeling fluid transfer along California faults when integrating pressure solution crack sealing and compaction processes. *J. Geophys. Res.* 108 (B2). doi:10.1029/2001JB000380
- Gratier, J.-P., Gueydan, F., 2007. Deformation in the presence of fluids and mineral reactions – Effect of fracturing and fluid–rock interaction on seismic cycles. In: Handy, M., Hirth, G., Hovius, N. (Eds.), *Tectonic Faults*. The MIT Press, Cambridge, Massachusetts, USA, pp. 319–356.
- Gratier, J.-P., Richard, J., Renard, F., Mitterperger, S., Doan, M.-L., Di Toro, G., Hadizadeh, J., Boullier, A.-M., 2011. Aseismic sliding of active faults by pressure solution creep: evidence from the San Andreas fault Observatory at depth. *Geology* 39, 1131–1134.
- Gratier, J.-P., 2011. Fault Permeability and strength evolution related to fracturing and healing episodic processes (Years to Millennia): the Role of pressure solution. *Oil Gas Sci. Technol. Rev. IFP Energies Nouvelles* 66 (3), 491–506.
- Heap, M.J., Faulkner, D.R., 2008. Quantifying the evolution of static elastic properties as crystalline rock approaches failure. *Int. J. Rock Mech. Min. Sci.* 45, 564–573.
- Hild, F., Denoual, C., Forquin, P., Brajer, X., 2003a. On the probabilistic-deterministic transition involved in a fragmentation process of brittle material. *Comp. Struct.* 81, 1241–1253.
- Hild, F., Forquin, P., Cordeiro da Silva, A.R., 2003b. Single and multiple fragmentation of brittle geomaterials. *Rev. Fr. Génie Civil* 7 (7–8), 973–1003.
- Irwin, G., 1957. Analysis of stresses and strain near the end of a crack traversing a plate. *Trans. ASME. Ser. E: J. Appl. Mech.* 24 (3), 361–364.
- Jayatilaka, A.de S., Trustrum, K., 1977. Statistical approach to brittle fracture. *J. Mat. Sci.* 12, 1426–1430.
- Kolsky, H., 1963. *Stress Waves in Solids*. Dover Publications.
- Mitchell, T.M., Ben-Zion, Y., Shimamoto, T., 2011. Pulverized fault rocks and damage asymmetry along the Arima-Takatsuki tectonic line, Japan: fault structure, damage distribution and textural characteristics. *Earth Planet. Sci. Lett.* 308 (3–4), 284–297.
- Mitchell, T.M., Faulkner, D.R., 2009. The nature and origin of off-fault damage surrounding strike-slip fault zones with a wide range of displacements: a field study from the Atacama fault system, northern Chile. *J. Struct. Geol.* 31 (8), 802–816.
- Nemat-Nasser, S., 2000. *Mechanical Testing and Evaluation*. In: ASM Handbook, vol. 8. ASM International, Ch. Introduction to high strain rate testing, pp. 427–428.
- Paterson, M.S., Wong, T.-F., 2005. *Experimental Rock Deformation – The Brittle Field*, second ed. Springer.
- Prentice, C.S., et al., 2009. Illuminating northern California's active faults. *EOS Trans. Amer. Geophys. U* 90 (7), 55.
- Rockwell, T.K., Sisk, M., Girty, G., Dor, O., Wechsler, N., Ben-Zion, Y., 2009. Granulometric and mineralogical properties of pulverized rocks from Tejon pass on the San Andreas fault and from Tejon Ranch on the Garlock fault, California. *Pure Appl. Geophys.* 166 (10–11), 1725–1746.
- Savage, H.M., Brodsky, E.E., 2011. Collateral damage: evolution with displacement of fracture distribution and secondary fault strands in fault damage zones. *J. Geophys. Res.* 116 (B3). doi:10.1029/2010JB007665
- Shi, Z., Ben-Zion, Y., 2006. Dynamic rupture on a bimaterial interface governed by slip-weakening friction. *Geophys. J. Int.* 165, 469–484.
- Vermilye, J.M., Scholz, C.H., 1998. The process zone: a microstructural view of fault growth. *J. Geophys. Res.* 103, 12223–12237.
- Wechsler, N., Allen, E.E., Rockwell, T.K., Girty, G., Chester, J.S., Ben-Zion, Y., 2011. Characterization of pulverized granitoids in a shallow core along the San Andreas fault, little rock, CA. *Geophys. J. Int.* 186, 401–407.
- Weibull, W., 1951. A statistical distribution function of wide applicability. *J. Appl. Mech. – Trans. ASME* 18, 293–297.
- Wessel, P., Smith, W.H.F., 1998. Improved version of Generic Mapping Tools released. *EOS Trans. Amer. Geophys. U* 79 (47), 579.
- Wilson, B., Dewers, T., Reches, Z., Brune, J., 2005. Particle size and energetics of gouge from earthquake rupture zones. *Nature* 434, 749–752.
- Yuan, F., Prakash, V., Tullis, T., 2011. Origin of pulverized rocks during earthquake fault rupture. *J. Geophys. Res.* 116, B06309.

Bibliography

- Bos, B., C. J. Peach, and C. J. Spiers (2000), Frictional-viscous flow of simulated fault gouge caused by the combined effects of phyllosilicates and pressure solution, *Tectonophysics*, *327*(3-4), 173–194.
- Caine, J. S., J. P. Evans, and C. B. Forster (1996), Fault zone architecture and permeability structure, *Geology*, *24*(11), 1025–1028.
- Candela, T., and F. Renard (2012), Segment linkage process at the origin of slip surface roughness: Evidence from the Dixie Valley fault, *Journal of Structural Geology*, *45*, 87–100, doi:10.1016/j.jsg.2012.06.003.
- Chen, W. W., and B. Song (2010), *Split Hopkinson (Kolsky) Bar Design, testing and applications*, Springer Verlag.
- Chester, F. M., and J. M. Logan (1986), Implications for mechanical properties of brittle faults from observation of the Punchbowl Fault Zone, California, *Pure and Applied Geophysics*, *124*(1/2), 79–106.
- Doan, M.-L., and A. Billi (2011), High strain rate damage of Carrara marble, *Geophysical Research Letters*, *38*(L19302), 1–6, doi:10.1029/2011GL049169.
- Doan, M.-L., and V. D’Hour (2012), Effect of initial damage on rock pulverization along faults, *Journal of Structural Geology*, *45*, 113–124, doi:10.1016/j.jsg.2012.05.006.
- Doan, M.-L., and G. Gary (2009), Rock pulverization at high strain rate near the San Andreas fault, *Nature Geoscience*, *2*(10), 709–712, doi:10.1038/ngeo640.
- Dor, O., T. K. Rockwell, and Y. Ben-Zion (2006), Geological Observations of Damage Asymmetry in the Structure of the San Jacinto, San Andreas and Punchbowl Faults in Southern California: A Possible Indicator for Preferred Rupture Propagation Direction, *Pure and Applied Geophysics*, *163*(2-3), 301–349, doi:10.1007/s00024-005-0023-9.
- Dor, O., C. Yildirim, T. K. Rockwell, Y. Ben-Zion, O. Emre, M. Sisk, and T. Y. Duman (2008), Geological and geomorphologic asymmetry across the rupture zones of the 1943 and 1944 earthquakes on the North Anatolian Fault: possible signals for preferred earthquake propagation direction, *Geophysical Journal International*, *173*(2), 483–504, doi:10.1111/j.1365-246X.2008.03709.x.
- Dunham, E. M., P. Favreau, and J. M. Carlson (2003), A Supershear Transition mechanism for cracks, *Science*, *299*, 1557–1559.
- Faulkner, D. R., C. A. L. Jackson, R. J. Lunn, R. W. Schlische, Z. K. Shipton, C. A. J. Wibberley, and M. Withjack (2010), A review of recent developments concerning the structure, mechanics and fluid flow properties of fault zones, *Journal of Structural Geology*, *32*(11), 1557–1575, doi:10.1016/j.jsg.2010.06.009.
- Gratier, J.-P., and F. Gueydan (2007), Deformation in the Presence of Fluids and Mineral Reactions Effect of Fracturing and Fluid – Rock Interaction on Seismic Cycles, chap. 12, pp. 319–356.
- Gratier, J.-P., J. Richard, F. Renard, S. Mittempergher, M.-L. Doan, G. Di Toro, J. Hadizadeh, and A.-M. Boullier (2011), Aseismic sliding of active faults by pressure solution creep: Evidence from the San Andreas Fault Observatory at Depth, *Geology*, *39*(12), 1131–1134, doi:10.1130/G32073.1.
- Mitchell, T. M., and D. R. Faulkner (2009), The nature and origin of off-fault damage surrounding strike-slip fault zones with a wide range of displacements: A field study from the Atacama fault system, northern Chile, *Journal of Structural Geology*, *31*(8), 802–816, doi:10.1016/j.jsg.2009.05.002.

- Mitchell, T. M., Y. Ben-Zion, and T. Shimamoto (2011), Pulverized fault rocks and damage asymmetry along the Arima-Takatsuki Tectonic Line , Japan, *Earth and Planetary Science Letters*, 308(3-4), 284–297, doi:10.1016/j.epsl.2011.04.023.
- Paterson, M. S., and T.-F. Wong (2005), *Experimental rock deformation—the brittle field*, Springer Verlag.
- Shi, Z., and Y. Ben-Zion (2006), Dynamic rupture on a bimaterial interface governed by slip-weakening friction, *Geophysical Journal International*, 165(2), 469–484, doi:10.1111/j.1365-246X.2006.02853.x.
- Sibson, R. H. (1992), Implication of fault-valve behaviour for rupture nucleation and recurrence, *Tectonophysics*, 211, 283–293.
- Wilson, B., T. A. Dewers, Z. Reches, and J. N. Brune (2005), Particle size and energetics of gouge from earthquake rupture zones Brent, *Nature*, 434, 749—752, doi:10.1029/2003GL019277.
- Yuan, F., V. Prakash, and T. E. Tullis (2011), Origin of pulverized rocks during earthquake fault rupture, *Journal of Geophysical Research*, 116(B6), 1–18, doi:10.1029/2010JB007721.